Thermal instability and vibration characteristics of laminated composite struts with Graphene reinforcements: An analysis of distribution patterns and geometrical imperfections

S.F. Nikrad [a], A.H. Akbarzadeh [b,c], M. Bodaghi [d], M. Hamidinejad [a], Z.T. Chen [a,*]

[a] Mechanical Engineering Department, University of Alberta, Edmonton, AB, Canada
[b] Bioresource Engineering Department, McGill University, Montreal H9 × 3V9, QC, Canada
[c] Mechanical Engineering Department, McGill University, Montreal H3A 0C3, QC, Canada
[d] Department of Engineering, School of Science and Technology, Nottingham Trent University, Nottingham NG11 8NS, UK

ARTICLE INFO

ABSTRACT

This study explores the effect of local buckling on the compressive performance of slender structural elements, particularly those with thin-walled sections. The phenomenon of local buckling significantly reduces the axial compressive stiffness, leading to a notable decrease in the load-bearing capacity of these elements. The main goal of this research is to examine how the post-buckling characteristics of polymeric composite channel section struts can be improved under thermal loading by incorporating multi-layer graphene reinforcements. The solution methodology incorporates the von Karman geometrical nonlinearity and is based on the layerwise third-order shear deformation theory (LW-TSDT). To ascertain the precision and computational performance of the results derived from LW-TSDT, a three-dimensional (3D) finite element model is created in ABAQUS for comparative evaluation. An extensive analysis of nonlinear thermal instability in perfect and geometrically imperfect FG-GRC laminated channel section struts is undertaken to discern the graphene distribution patterns that are most and least effective in elevating the critical buckling temperature and natural frequencies through pre- and post-buckling conditions. The comparative analysis indicates that employing the FG-X graphene distribution pattern across the thickness of the web and flanges in channel section struts leads to a projected increase of 12 % in the critical buckling temperature for clamped channel section struts, in contrast to those that adopt the FGO graphene distribution pattern. For cases with simply-supported boundary conditions, this increase is noted to be approximately 9 %. Moreover, findings confirm that incorporating an asymmetric graphene distribution pattern (FGV) or introducing geometrical imperfections in the flanges and web that generate a bending moment within the structure from the beginning of thermal loading effectively prevents the primary natural frequencies of FG-GRC channel section struts from declining to zero close to the critical buckling temperature. This is significantly different from scenarios involving perfectly structured and symmetrically reinforced graphene distribution patterns such as FGX.

1. Introduction

1.1. Graphene as a composite reinforcement

The domain of nanoscience has experienced significant expansion in the last twenty years, with nanotechnology coming to the forefront in areas like electronics, biomedicine, and energy. Within this framework, the identification and incorporation of graphene into polymer nano-composites marks a notable achievement in nanoscience. Composed of carbon atoms in a hexagonal lattice, graphene is an atomic-scale layer that demonstrates a variety of extraordinary characteristics [1–6]. These include the high carrier mobility at room temperature (approximately 10,000 cm^{2}V^{-1}S^{-1}) [7], large theoretical specific surface area (2630 m^{2}g^{-1}) [8], excellent optical transparency (approximately 97.7 %) [9], high Young's modulus (around 1 TPa) [10], and outstanding thermal conductivity (ranging from 3000 to 5000 Wm^{-1}K^{-1}) [11]. When compared to other nanomaterials, graphene displays superior multi-functional properties.

Molecular dynamic (MD) simulations are frequently used to clarify the properties of different carbon-based materials, such as graphite, fullerenes, and nanotubes [10–18]. MD simulations have confirmed that changes in the size of graphene sheets do not affect their anisotropic Young's modulus [15]. Owing to its wide array of uses and impressive tensile strength, this fascinating material has now reached a point where its effective integration into polymer nanocomposites is feasible. This advancement is significant, as it opens up new possibilities in various fields where the unique properties of graphene can enhance the performance of polymer-based materials. By blending graphene with polymers, we can create composites that are not only stronger and more durable but also have enhanced electrical and thermal properties, making them suitable for innovative applications in electronics, automotive, aerospace, and other high-tech industries [19]. Unlike composites reinforced with carbon fibers, where a substantial amount of carbon fibers can be included, composites reinforced with graphene (GRCs) have a limited capacity for adding nanofillers, typically ranging from 0.05 to 5 wt percent. This difference is mainly due to the distinct structural and physical properties of graphene compared to traditional carbon fibers. Graphene's high surface area and strength allow it to provide significant reinforcement even at lower concentrations. Moreover, adding too much graphene can lead to agglomeration and a decrease in overall composite performance [20–22].

Due to existing technological challenges, the fabrication of functionally graded materials (FGM) with an ideal and flawless transition between two distinct material phases remains a complex task. As a practical alternative, a multilayered structure, comprising several layers each demonstrating a gradual shift in the blend proportion between the matrix and nano-reinforcement materials, presents a viable solution [23]. For the construction of multilayer or graded composites, graphene platelets (GPLs) are utilized to strengthen the composite matrix. GPLs consist of multiple, parallel layers of two-dimensional graphene. The manufacturing process involves mixing epoxy, which acts as the composite's matrix, with specific weight percentages of graphene platelets. Typically, this blend is poured into a mold to form the initial layer. This process is repeated in a sequential manner to fabricate additional layers of the nanocomposite, each with different proportions of GPLs. Ultimately, these individual layers are fused together to form a cohesive structure [23].

Integrating graphene sheets into a polymer matrix enables fine-tuning of the mechanical, thermal, and electrical characteristics of composite materials. This structured distribution of graphene not only lightens the composite's weight but also makes it appropriate for lightweight applications without compromising structural strength and multifunctional capabilities. Numerous experimental and computational studies have been conducted to investigate the impact of using graphene sheets as reinforcements, especially with different graded distribution patterns, on the static and dynamic properties of engineering structures.

A multitude of research endeavors has been dedicated to examining laminated beams composed of graphene-epoxy nanocomposites. The findings from these studies uniformly indicate that a marginal elevation in the weight proportion of graphene markedly boosts the critical buckling load of these beams. Remarkably, the incorporation of a mere 0.1 % weight fraction of graphene platelets has been observed to escalate the critical buckling load by an astounding 52 % when contrasted with beams fabricated exclusively from epoxy [24]. Furthermore, extensive numerical analyses, [25–29], have been conducted to examine the nonlinear bending, thermal post-buckling, and dynamic instability in laminated nanobeams reinforced with graphene. These studies employed the Timoshenko beam theory and considered the von-Karman nonlinear strain-displacement relationshiThe primary objective of these numerical studies was to elucidate the significant influence of the volume fraction and distribution pattern of graphene reinforcement on the nonlinear behavior of the nanobeams.

The buckling behavior of a single-layer graphene/epoxy composite plate, sized at 23.79×12 nm, was evaluated employing the multiscale volume element method. The study featured atomistic-level modeling of graphene and a continuum-based analysis for polymer deformation. The findings reveal a substantial enhancement in the critical buckling load of the nanocomposite plate, registering a 26 % increase due to the integration of a 6 % volume fraction of graphene [30]. Another noteworthy outcome from recent numerical analysis that investigated the nonlinear bending [31], thermal post-buckling [32–35], and nonlinear vibration [36–38] responses of FG-GRC laminated plates is that a symmetric FG-X distribution pattern demonstrates superior performance in terms of critical buckling temperature and natural frequency when compared to other symmetric and asymmetric distribution patterns. In this particular symmetric arrangement of graphene, the topmost layer contains the highest concentration of graphene reinforcement. Progressing towards the midplane, there is a consistent reduction in the volume percentage of graphene, leading to the central composite layer that has the minimal graphene content. This gradient in graphene distribution is critical to the enhanced structural performance observed in this configuration.

Considerable advancements in manufacturing techniques have markedly transformed the creation of advanced materials, culminating in the achievement of outstanding thermoelectromechanical properties. This evolution in production technology has notably enabled the fabrication of innovative lightweight auxetic materials, distinguished by their extraordinary negative Poisson's ratio (NPR) [39–41]. The fusion of remarkable characteristics inherent to architecturally derived materials and the superior properties of nanomaterials presents a promising avenue for enabling the creation of next-generation, high-performance, architected composites utilizing nanomaterials. This synergy harnesses the distinct architectural design elements and the advanced capabilities of nanomaterials to push the boundaries of composite structure performance [41]. For example, the compressive and thermal post-buckling behavior of sandwich plates and cylindrical panels with an auxetic graphene-reinforced metal matrix composite (GRMMC) core have been examined by many researchers [42–44], and the results confirmed that the FG pattern of the graphene sheets combined with the auxeticity of the cellular core can impart structures with enhanced buckling resistance. As an intriguing avenue for designing nano-architected metamaterials inspired by the art of paper folding, graphene or graphene layers can also be folded to form cellular origamis that offer tailorable multifunctional properties, from auxeticity and foldability to tunablity of mechanical and thermoelectric and properties [45,46].

1.2. Thin-walled composite laminated struts

Recent years have seen a notable expansion in the application of composite laminates across diverse sectors, attributed to their ability to strike an optimal balance between stiffness, strength, and weight. Concurrently, advancements in manufacturing technologies, particularly 3D printing, have significantly transformed the fabrication of composite laminates. This evolution offers substantial advantages in design flexibility, customization, and production efficiency. The integration of 3D printing capabilities with the benefits of composite materials represents a pioneering methodology, opening new opportunities for constructing intricate and functional engineering structures, including thin-walled composite laminated struts [47,48].

These structures find frequent application in contexts requiring in-plane compressive loading, especially prevalent in the aerospace sector. The industry's drive towards engineering efficient and lightweight structures necessitates an assessment of local buckling and post-buckling behaviors at specific critical buckling loads. Conducting a meticulous analysis of compressive instability is imperative for these structures due to the significant diminution in compressive stiffness and load-bearing capacity observed during the post-buckling phase. This advanced understanding is critical to ensure structural integrity and performance under operational conditions [49]. Consequently, a comprehensive array of research endeavors, encompassing numerical

simulations, analytical techniques, and experimental studies, has been conducted on thin-walled struts with open and closed sections. These studies have focused on a variety of sectional geometries, employing a range of isotropic and anisotropic materials to evaluate their characteristics precisely [49–74].

A cutting-edge P-version technique was developed to create a comprehensive 3D finite element model (FEM) for analyzing local, overall, and interactive buckling behaviors in thin-walled structures. This model encompassed various sectional geometries, including channel sections, box, and I-sections. A pivotal discovery of this research was the substantial impact of the length-to-web width ratio (L / B_w) on buckling types. Specifically, in short struts with an L / B_w ratio approximately equal to 1, a predominant local buckling mode was noted. Conversely, at lower L/B_w ratios, a transition between local and overall buckling modes was observed, resulting in an interactive buckling mode shape [68].

An analytical assessment of the local buckling behavior in fiber-reinforced composite laminated beams under uniform compressive load was performed for various sectional geometries, such as I, C, Z, T, and L configurations, utilizing two distinct methodologies [55,56,58, 62]. The first method involved a segmented analysis of the beam's components, like flanges and webs, employing an energy-based semi-analytical technique with elastic rotational constraints at the flange-web junction. Conversely, alternate research introduced an integrated approach using the Ritz method, which conducted a collective analysis of webs and flanges as a unified system, implementing precise continuity conditions at the interconnections of webs and flanges. Both approaches provided closed-form formulas to determine key quantities, such as the critical buckling load. This characteristic renders these two approaches highly valuable and practical from an engineering standpoint.

Finite element analysis (FEA) was employed to evaluate the influence of geometrical imperfections and elastoplastic material characteristics on the post-buckling behavior, compressive stiffness, and structural failure of thin-walled I and box section struts [57]. The aim was to precisely compare the axial compressive stiffness variations under elastic circumstances against those in situations incorporating material nonlinearity. A comprehensive series of experimental tests were meticulously conducted on thin-walled struts, characterized by their complex cross-sectional profiles and the inclusion of multiple intermediate stiffeners. The obtained strength test results were compared with numerical simulations, validating the finding that the presence of intermediate stiffeners increases the local buckling stress level [60]. The application of the exact finite strip method (FSM) was implemented to analyze the local buckling and initial post-buckling characteristics of thin-walled I-section struts [59]. In addition, the evaluation of post-buckling stiffness and the geometrically nonlinear behavior of channel section struts was executed using two specialized analytical techniques: the semi-energy and the full-energy FSM [49,73]. In the first method, only the out-of-plane displacement is specified, while the second method incorporates both in-plane and out-of-plane displacement functions from the very beginning of the computational process. It is worth noting that in a compelling previous study, the influence of interlaminar defects, delamination, on the post-buckling characteristics of fiber-reinforced composite laminated angle section and T-section struts was rigorously analyzed based on the layerwise theory. This detailed examination disclosed that delamination occurring amongst the flange layers markedly decreased the load-bearing capacity of these laminated composite thin-walled structures [57].

In conclusion, an exhaustive review of the literature clearly demonstrates that local buckling must be considered as a paramount design factor for thin-walled struts, regardless of their cross-sectional configuration. Local buckling significantly influences the axial compressive stiffness and consequently adversely affects the load-bearing capacity. Therefore, it is essential to prioritize addressing this crucial issue in such widely used engineering structures, through detailed evaluation of various strategies to ascertain effective solutions.

To address the complex behavior of slender structural elements under compressive and thermal loads, this study introduces novel methodologies and findings that significantly extend the current understanding of local buckling phenomena of these structures. Unlike previous research, which primarily focused on conventional materials and reinforcements, this study uniquely explores the incorporation of multi-layer graphene into polymeric composite structures. This approach leverages the distinctive thermal and mechanical properties of graphenes to enhance the buckling resistance and load-bearing capabilities of thin-walled channel section struts. Furthermore, the employment of the layerwise, third-order shear deformation theory (LW-TSDT) combined with a sophisticated three-dimensional finite element model in ABAQUS represents a significant advancement in the capabilities of analytical methods for tackling such problems. By comparing different graphene distribution patterns and introducing geometrical imperfections, this study provides new insights into optimizing structural resilience against thermomechanical buckling.

This research conducts a comparative analysis of various arrangements of functionally graded graphene sheets, distributed along the thickness directions of the flanges and web plates in channel section struts. The aim is to identify the specific pattern combinations that most effectively enhance the critical buckling temperature, as well as the fundamental and second-order frequencies, in both pre- and post-buckling states. Alongside examining various material configurations and conducting an in-depth comparison of the thermal post-buckling characteristics between the most and least impactful cases against the uniform distribution (UD) graphene pattern, this study also assesses how boundary conditions and localized geometrical imperfections, applied either individually or collectively to each flange and web, influence the thermal instability response and variation of pre- and post-buckled frequencies.

To fulfill the research goals effectively, an advanced, layerwise theoretical model based on the third-order shear deformation theory (TSDT) is developed. This innovative approach is instrumental in analyzing the thermal and mechanical instability responses of thin-walled structures. The initial step in this methodology involves treating the constituent plates (including flanges and web) as separate, distinct elements. This is followed by a discretization process, wherein each plate is segmented into several numerical layers along its thickness. A pivotal element of this method is the establishment of displacement and rotation shape functions at the midplane of each layer. It is crucial to underscore the importance of ensuring these shape functions adhere rigorously to the continuity and boundary conditions that govern the structural entirety. Moreover, a 3D finite element model is implemented, utilizing the commercial software ABAQUS, to incorporate some of the findings derived from the LW-TSDT. Additionally, this study presents a comparative evaluation of the central processing unit (CPU) time required by both methodologies. These approaches demand differing quantities of displacement and rotational degrees of freedom (DOFs) to precisely evaluate the nonlinear behavior observed in channel section struts.

2. Basic theoretical formulations

The current study delves into the structure of multilayer laminated composite channel section struts, comprising several subcomponents such as two vertical plates (named flange1&2) and a horizontal plate (termed the web), as shown in Fig. 1. Measurements for both flanges and the web are expressed in terms of thickness and width, denoted by t_f, b_f, t_w, and b_w, respectively. The strut's total length is represented as L. Additionally, Fig. 1 illustrates the setup of a local Cartesian coordinate system, centered at the mid-plane of each structural subelement. These coordinate systems are crucial for the formulation of accurate displacement and rotational shape functions within the study.

As highlighted earlier, each structural subcomponent, encompassing flanges and web, is composed of N distinct composite layers. These
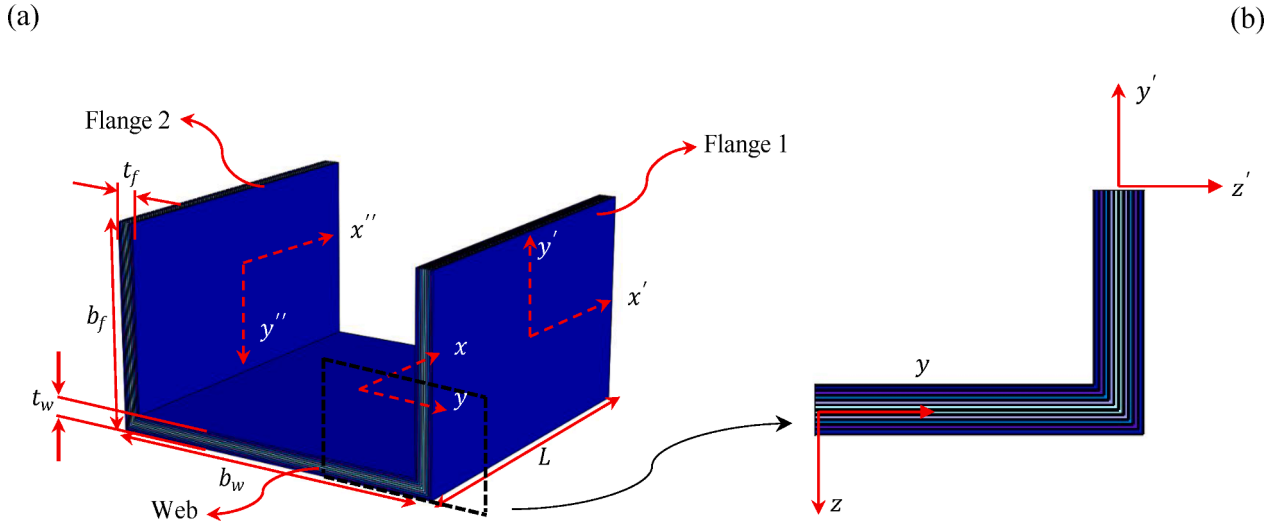
Fig. 1. (a) A schematic FG-GRC laminated channel section struts with their local coordinate systems (b) detailed view half of the piecewise functionally graded graphene reinforced cross-section.

layers consist of a polymeric matrix integrated with graphene sheets, where the concentration of graphene varies. This variation gives rise to a complex laminated construct termed a piecewise functionally graded graphene-reinforced composite. Within the scope of this research, two primary graphene reinforcement configurations are examined: the zigzag pattern (designated as 0°-ply) and the armchair pattern (identified as 90°-ply). The focus of this article is a comprehensive analysis and evaluation of six unique non-uniform graphene distribution patterns, assessing their reinforcement efficacy relative to the uniformly distributed (UD) graphene arrangement. The studied non-uniform patterns encompass four symmetric distributions (namely FG-X, FGX-FGX, FG-O, and FGO-FGO) and two asymmetric distributions (FG-V and FGV-FGV), as detailed in Table 1.

Table 1 features a color-coded representation of the layers, indicating the volume fraction of graphene sheets within each. In this scheme, a darker blue signifies layers containing the highest graphene volume fraction (0.11), whereas a lighter blue designates layers with the minimal graphene content (0.03). Additionally, the subscripts "2″" and "s″" are employed to describe two specific attributes. The subscript "2″" denotes the count of layers having an identical graphene volume fraction, distributed from the topmost to the bottommost layer. Conversely, the subscript "s″" is used to represent the symmetric distribution of graphene reinforcement across the thickness of the plate.

Different permutations of the graphene distribution patterns detailed in Table 1 can be independently selected for the flanges and the web. For better understanding, Fig. 2 provides illustrative representations of channel section struts, showcasing instances where both the flanges and the web employ an identical FGX graphene distribution pattern.

The comprehension of thermomechanical properties in GRCs plays a pivotal role in evaluating their structural functionality. To determine these properties with precision in polymer nanocomposites that are reinforced with graphene, MD simulations have been effectively utilized [75]. A critical comparison between the outcomes of these MD simulations and the predictions made by both the Halpin-Tsai model [76] and the rule of mixtures [75] reveals a notable mismatch. This indicates that the conventional micromechanical models are somewhat limited in their ability to accurately capture the effective material properties of GRCs, especially due to nano-scale size and surface effect. Therefore, there is a recognized need for modification and refinement of these models [32].

To tackle this challenge, the Halpin-Tsai mathematical framework has been refined to account for varying volume fractions of graphene sheets through the incorporation of efficiency parameters. These parameters are $\eta_i, \ i = 1, 2, 3$ calibrated at different temperatures, ensuring

alignment between the outcomes of MD simulations and the revised Halpin-Tsai model. This methodology enables an evaluation of both the elastic and shear modulus of the composite medium, which is reinforced with graphene sheets, as elucidated in reference [31].

$$E_{11} = \eta_1\left(V^G, T\right) \frac{1 + 2\left(\frac{a^G}{h^G}\right)\gamma_{11}V^G}{1 - \gamma_{11}V^G}E^m(T)$$

$$E_{22} = \eta_2\left(V^G, T\right) \frac{1 + 2\left(\frac{b^G}{h^G}\right)\gamma_{22}V^G}{1 - \gamma_{22}V^G}E^m(T)$$

$$G_{12} = \eta_3\left(V^G, T\right) \frac{1}{1 - \gamma_{12}V^G}G^m(T) \tag{1}$$

where a^G, b^G, and h^G, represent the length, width, and effective thickness of the graphene sheet, respectively. The remaining supplementary parameters are as defined by [31,35]:

$$\gamma_{11} = \frac{\left(\frac{E_{11}^G(T)}{E^m(T)}\right) - 1}{\left(\frac{E_{11}^G(T)}{E^m(T)}\right) + 2\left(\frac{a^G}{h^G}\right)}$$

$$\gamma_{22} = \frac{\left(\frac{E_{22}^G(T)}{E^m(T)}\right) - 1}{\left(\frac{E_{22}^G(T)}{E^m(T)}\right) + 2\left(\frac{b^G}{h^G}\right)}$$

$$\gamma_{12} = \frac{\left(\frac{G_{12}^G(T)}{E^m(T)}\right) - 1}{\left(\frac{G_{12}^G(T)}{E^m(T)}\right)} \tag{2}$$

It is important to acknowledge that E^m and G^m symbolize the moduli of elasticity and shear, respectively, pertaining to the uniform isotropic matrix. Furthermore, in Eq. (2), the terms E_{11}^G, E_{22}^G, and G_{12}^G correspond to the elastic and shear moduli of the graphene sheets. Reflecting on the composition of each GRC laminate layer, which includes both graphene and the matrix, Eq. (1) uses V^G to represent the volume fraction of graphene, while V^m, defined as $1\text{-}V^G$, reflects the proportional volume of the matrix. The Schapery model [75] is widely recognized and employed

Table 1
Lay-up arrangements of the FG-GRC laminated plates with different graded graphene distributions.

Graphene distribution patterns	Lay-up arrangements of graphene volume fraction	Schematic distribution patterns
FG-X	$[0.11, 0.09, 0.07, 0.05, 0.03]_s$	
FGX-FGX	$[0.09, 0.07, 0.03, 0.07, 0.09]_s$	
FG-O	$[0.03, 0.05, 0.07, 0.09, 0.11]_s$	
FGO-FGO	$[0.05, 0.07, 0.11, 0.07, 0.05]_s$	
FG-V	$[(0.11)_2, (0.09)_2, (0.07)_2, (0.05)_2, (0.03)_2]$	
FGV-FGV	$[0.11, 0.09, 0.07, 0.05, 0.03, 0.11, 0.09, 0.07, 0.05, 0.03]$	

for calculating the coefficients of thermal expansion in composite materials, including those reinforced with carbon nanotubes. This model is equally relevant and applicable to the analysis of GRC materials.

$$\alpha_{11} = \frac{V^G E_{11}^G(T) \alpha_{11}^G(T) + V^m E^m(T) \alpha^m(T)}{V^G E_{11}^G(T) + V^m E^m(T)}$$

$$\alpha_{22} = \left(1 + \nu_{12}^G(T)\right) V^G \alpha_{22}^G(T) + \left(1 + \nu^m(T)\right) V^m \alpha^m(T) - \nu_{12}(T) \alpha_{11}(T) \quad (3)$$

where α_{11}^G, α_{22}^G and α^m are the thermal expansion coefficients, and ν_{12}^G and ν^m are the Poisson's ratios, respectively, of the graphene sheet and matrix. The Poisson's ratios of the GRCs can be expressed in terms of the Poisson' ratios of constituents according to the standard rule of mixes [75]. As a result, one may arrive at:

$$\nu_{12} = V^G \nu_{12}^G(T) + V^m \nu^m(T) \quad (4)$$

The Generalized Higher Order Shear Deformation Theory (GHSDT) represents an advanced theoretical approach for examining the behavior of thin-walled structures subject to bending, buckling, and vibrational forces. Diverging from traditional plate theories, GHSDT introduces higher-order displacement variables, coupled with the presumption of a linear variation in shear strains across the thickness of the plate. A more refined and streamlined variant of GHSDT is the Third-Order Shear Deformation Theory (TSDT). The TSDT framework limits itself to third-order displacement terms while maintaining the assumption of linear shear strain variation. Renowned for its precision in predicting the responses of thin-walled structures under diverse load conditions and boundary constraints, TSDT has become a staple in various engineering disciplines for its practical efficacy [77].

In the field of laminated plate theories, essential for analyzing plates and shells, there are two main methodologies: the Equivalent Single Layer (ESL) theory and the Layerwise theory. Both approaches simplify the complex 3D elasticity challenges into a more manageable two-dimensional (2D) format, as referenced in [78,79]. Yet, the ESL theory faces particular limitations, especially in accurately capturing stress and strain distributions in thick composite laminates or in cases with layers of dissimilar materials, like FG-GRC, where thermomechanical properties vary across the thickness. This limitation stems from its assumption of uniform transverse shear stresses throughout the thickness. To overcome these challenges and precisely determine the post-buckling behavior of FG-GRC laminated channel section struts, this research utilizes the Layerwise theory in conjunction with the TSDT. This approach marks a pioneering effort in analyzing such thin-walled structures using this combined methodology.

The TSDT-based formulation of displacement fields for individual numerical layers, defined under the layerwise theory, within the FG-GRC laminated composite channel section struts, whether in the web or flange, can be expressed as follows [77]:

$$u_j^i(x,y,z,\,t) = u_{j,0}^i(x,y,t) + \theta_j^i(z)\varphi_{j,x}^i(x,y,t) + \gamma_j^i(z)\psi_{j,x}^i(x,y,t)$$

$$v_j^i(x,y,z,t) = v_{j,0}^i(x,y,t) + \theta_j^i(z)\varphi_{j,y}^i(x,y,t) + \gamma_j^i(z)\psi_{j,y}^i(x,y,t)$$

$$w_j^i(x,y,z,t) = w_{j,0}^i(x,y,t) + w^*(x,y,t) \quad (5)$$

As illustrated in Fig. 3, $u_{j,0}^i$, $v_{j,0}^i$, and $w_{j,0}^i$ represent the displacement components defined at the midplane of the ith numerical layer located at the jth region including flange 1 and 2 or web; $\varphi_{j,x}^i$ and $\varphi_{j,y}^i$ are also the middle surface rotations of those regions around the Y and X axes, respectively. Additionally, $\psi_{j,x}^i$ and $\psi_{j,y}^i$ denote the higher-order terms related with Taylor series. These parameters can be written as:

$$\psi_{j,x}^i = \frac{\partial w_j^i}{\partial x}, \ \psi_{j,y}^i = \frac{\partial w_j^i}{\partial y}, \ \theta_j^i(z) = z - \frac{4z^3}{3h_j^{i2}}, \ \gamma_j^i(z) = -\frac{4z^3}{3h_j^{i2}}, \ \varphi_{j,x}^i = \frac{\partial u_j^i}{\partial z}, \ \varphi_{j,y}^i$$

$$= \frac{\partial v_j^i}{\partial z}$$

$$(6)$$

For the sake of brevity, the von-Karman nonlinear strain–displacement and linear stress-stress relations, as well as stiffness matrix equations are given in Appendix A.

3. Structural modelling of channel section struts

3.1. Modelling based on the LW-TSDT

Within the scope of layerwise theory, it's imperative to divide the flanges and web plates into a series of numerical layers, aligned with their thickness. The number of these layers may equal, exceed, or be
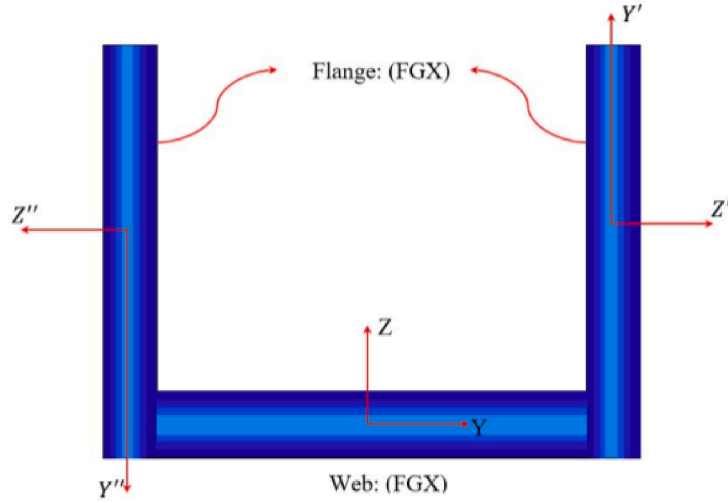
Fig. 2. Schematic depiction of the cross-section with an FGX graphene distribution pattern within both the flanges and the web.

fewer than the actual number of graphene-reinforced polymer composite layers comprising the flanges and web. Notably, increasing the count of numerical layers tends to enhance result accuracy. However, this advantage is balanced by a corresponding increase in computational load and CPU resource consumption. The layerwise theory necessitates unique rotational functions around the X and Y axes for each segmented layer. In this research, the in-plane and out-of-plane displacement functions at the midplane of each numerical layer are accurately defined according to the TSDT.

Fig. 3 presents a detailed schematic of the methodical steps required for the precise application of the Layerwise Third-Order Shear Deformation Theory (LW-TSDT). The process begins by dividing the FG-GRC channel section strut into three separate components: two flanges and one web. Each component is assigned its own local coordinate system, centered at the midplane. The next phase involves the stratification of each component into a variable number of numerical layers along their thickness. In this phase, each segmented layer is treated analogously to a distinct plate. This facilitates the establishment of rotational and displacement shape functions at the midplanes of these layers, consistent with the tenets of the TSDT. It's essential for the shape functions to precisely conform to the continuity conditions where adjacent numerical layers meet. They must also align with the boundary conditions at the channel section struts' longitudinal ends. While our theoretical framework accommodates different types of edge supports, this particular analysis is focused on FG-GRC channel section struts with clamped and simply-supported boundary conditions at both ends, as mathematically outlined in Table 2.

At the conclusion of the process, the three components, two flanges and one web, are integrated to create a unified structure for analytical purposes. A critical factor in this integration is the verification that the rotational and displacement functions, established in the preceding step, meet the continuity condition at the junction where the flange and web plates intersect and connect.

The adoption of an in-plane stress-free edge as a continuity condition at the flange-web junction in various open section struts is a prevalent practice. This approach significantly enhances the alignment of both analytical and numerical methods with real-world conditions, especially in the study of their nonlinear post-buckling behavior. In the context of this study, the condition applied permits the nodes at the junction of the flanges and web plates to move freely within the plane, while their out-of-plane displacements are constrained. For any given point along the junction's length, there exist two overlapping nodes. One node pertains to the flange and the other is linked to the web plate. The imposed continuity condition here ensures that the in-plane displacement of these nodes in the X-direction is identical, and they share an equal

rotation about the X and Y-axes. The in-plane stress-free edge condition essentially implies that following the local buckling of wall sections, the junctions maintain their flatness without experiencing any out-of-plane displacements. The mathematical representation of this condition is expressed as follows:

$$\left(u_f^{(i)}, \varphi_{xf}^{(i)}, \varphi_{yf}^{(i)}\right)\Big|_{y=\frac{-b_f}{2}} = \left(u_w^{(i)}, \varphi_{xw}^{(i)}, \varphi_{yw}^{(i)}\right)\Big|_{y=\frac{b_w}{2}}, \ \{i=1..n\}$$

$$\left(u_f^{(i)}, \varphi_{xf}^{(i)}, \varphi_{yf}^{(i)}\right)\Big|_{y''=\frac{b_f}{2}} = \left(u_w^{(i)}, \varphi_{xw}^{(i)}, \varphi_{yw}^{(i)}\right)\Big|_{y=\frac{-b_w}{2}}, \ \{i=1..n\}$$

$$w_w^{(i)}\Big|x=\frac{-L_1}{2} = w_w^{(i)}\Big|x=\frac{L_1}{2} = w_w^{(i)}\Big|y=\frac{-b_w}{2} = w_w^{(i)}\Big|y=\frac{b_w}{2} = 0, \ \{i=1..n\}$$

$$w_f^{(i)}\Big|y'=\frac{-b_f}{2} = w_f^{(i)}\Big|y''=\frac{b_f}{2} = 0, \ \{i=1..n\} \tag{7}$$

These factors contribute to the increased complexity involved in designing the rotational and displacement functions for FG-GRC channel section struts. In Eq. (7), indexes "f" and "w" associated with the flange and web, respectively. For instance, $\left(u_f^{(i)}, \ w_f^{(i)}\right)$ and $\left(u_w^{(i)}, \ w_w^{(i)}\right)$ represent the in-plane and out-of-plane displacements of the ith numerical layer located through the thickness of the flange and web, respectively. Additionally, $(\varphi_{xf}^{(i)}, \varphi_{yf}^{(i)})$ and $(\varphi_{xw}^{(i)}, \varphi_{yw}^{(i)})$ correspond to the midplane rotation of the ith numerical layer of the flange and web, respectively.

As expressed in Eq. (7), all these rotational and displacement shape functions are defined according to the local coordinate systems established at the mid-plane center of the flanges and web plates.

Table 2 elucidates that the fundamental difference between clamped and simply-supported boundary conditions is confined solely to the rotation of the flanges and web about the local Y-axis ($\varphi_{xw}^{(i)}, \ \varphi_{xf}^{(i)}$). In contrast, all other shape functions, including in-plane and out-of-plane displacements, as well as rotations around the X-axis, are consistent across both types of boundary conditions. Following this, the viable functions for out-of-plane displacements under both clamped and simply-supported conditions are determined in accordance with Eq. (8).

$$w_w^{(1)} = \sum_{m=0}^{M} \sum_{n=0}^{N} \left(x - \frac{L}{2}\right)\left(x + \frac{L}{2}\right)\left(y + \frac{b_w}{2}\right)\left(y - \frac{b_w}{2}\right) w_{w,mn}^{(1)} x^m y^n, \ w_w^{(1)}$$
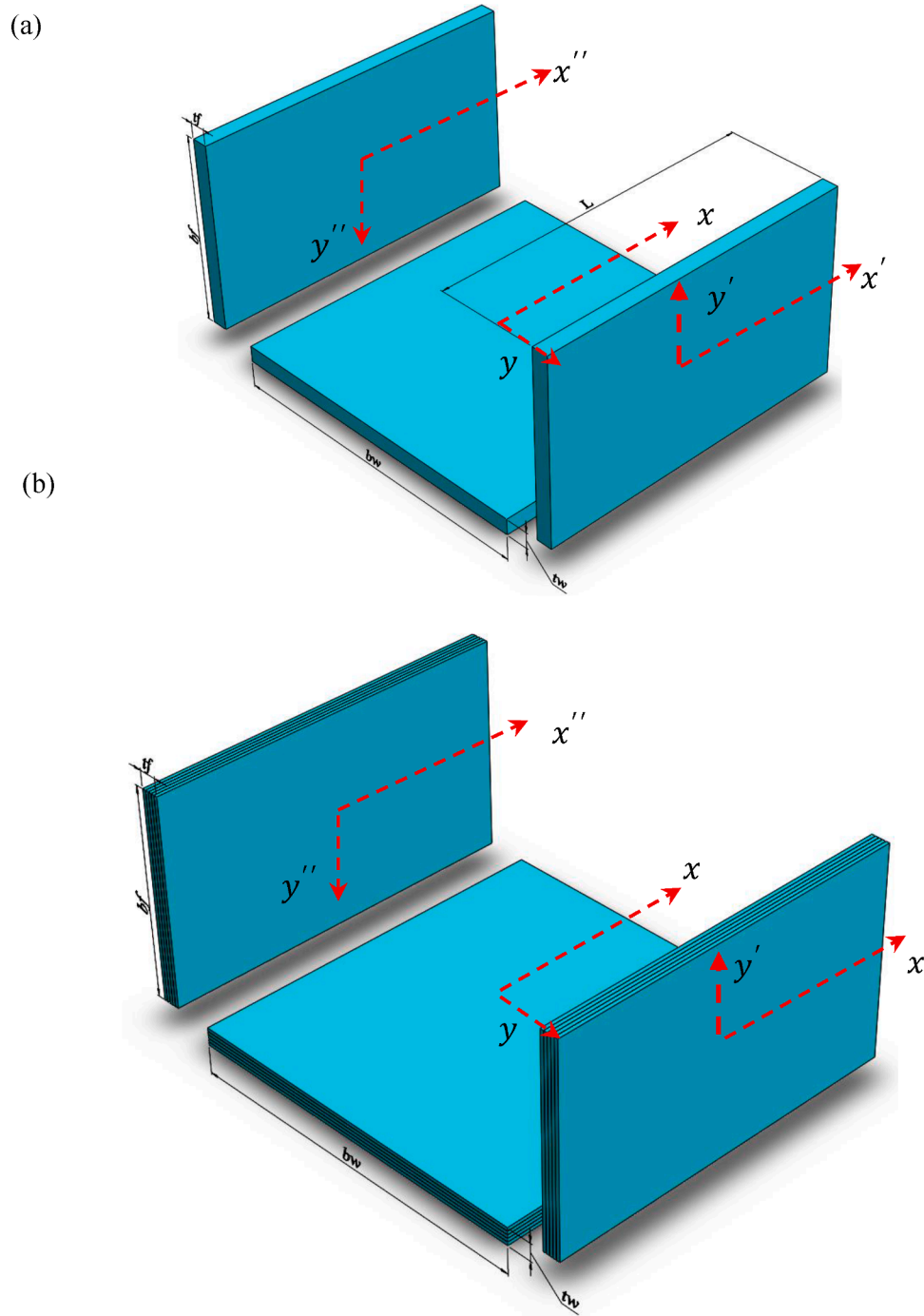$$= w_w^{(i)} \ i = 2..n$$

(a)

(b)

Fig. 3. A typical channel section strut and segmentation of the flanges and web (a) Separation of flanges and web, (b) Discretization of flanges and web through their thickness based on the layerwise theory.

Table 2
Mathematical expressions of the boundary conditions at longitudinal ends of the FG-GRC channel section struts.

Boundary condition		Out-of-plane displacement	Rotation
clamped	Flange	$w_f^{(i)}\|x = \frac{-L_1}{2} = w_f^{(i)}\|x = \frac{L_1}{2} = 0 \, i = 1..n$	$\varphi_{xf}^{(i)}\|x = \frac{-L_1}{2} = \varphi_{xf}^{(i)}\|x = \frac{L_1}{2} = 0 \, i = 1..n$
	Web	$w_w^{(i)}\|x = \frac{-L_1}{2} = w_w^{(i)}\|x = \frac{L_1}{2} = 0 \, i = 1..n$	$\varphi_{xw}^{(i)}\|x = \frac{-L_1}{2} = \varphi_{xw}^{(i)}\|x = \frac{L_1}{2} = 0 \, i = 1..n$
simply-supported	Flange	$w_f^{(i)}\|x = \frac{-L_1}{2} = w_f^{(i)}\|x = \frac{L_1}{2} = 0 \, i = 1..n$	$\varphi_{xf}^{(i)}\|x = \frac{-L_1}{2} \& \varphi_{xf}^{(i)}\|x = \frac{L_1}{2} \neq 0 \, i = 1..n$
	Web	$w_w^{(i)}\|x = \frac{-L_1}{2} = w_w^{(i)}\|x = \frac{L_1}{2} = 0 \, i = 1..n$	$\varphi_{xw}^{(i)}\|x = \frac{-L_1}{2} \& \varphi_{xw}^{(i)}\|x = \frac{L_1}{2} \neq 0 \, i = 1..n$

$$w_{f1}^{(1)} = \sum_{m=0}^{M} \sum_{n=0}^{N} \left(x - \frac{L}{2}\right)\left(x + \frac{L}{2}\right)\left(y' + \frac{b_f}{2}\right) w_{f1,mn}^{(1)} x^m y^n, \quad w_{f1}^{(1)} = w_{f1}^{(i)} \, i$$
$$= 2..n$$

$$w_{f2}^{(1)} = \sum_{m=0}^{M} \sum_{n=0}^{N} \left(x - \frac{L}{2}\right)\left(x + \frac{L}{2}\right)\left(y'' - \frac{b_f}{2}\right) w_{f2,mn}^{(1)} x^m y^n, \quad w_{f2}^{(1)} = w_{f2}^{(i)} \, i$$
$$= 2..n \tag{8}$$

Eq. (8) clearly indicates that the out-of-plane displacements of both the web and flanges (w_w, w_f) are restricted along their longitudinal boundaries ($x = \frac{L}{2}$, $x = -\frac{L}{2}$), adhering to the specified boundary conditions. As detailed earlier, these conditions require either clamping or simply-support of the channel section strut at its longitudinal ends. Additionally, the equation highlights that in order to meet the continuity conditions at the junctions of the web and flanges $\left(\textbf{at } \boldsymbol{y = \frac{b_w}{2}, \, y = -\frac{b_w}{2}},\right.$ $\left. \boldsymbol{y' = -\frac{b_f}{2}, \, \text{and } y'' = \frac{b_f}{2}} \right)$, where it is assumed that these intersections remain flat following the post-buckling deflection, the out-of-plane displacements of both the web and flanges are also required to be constrained at these specific points.

Assuming the absence of interlaminar imperfections like delamination between the graphene-reinforced composite layers of both flanges and web, it is observed that each ply within these areas experiences the same out-of-plane displacement when subjected to bending. This leads to the assumption that the out-of-plane displacements for all discretized numerical layers in each flange or web section are consistent. Ensuring this consistency is vital for fulfilling the continuity condition along the out-of-plane interfaces of the numerical layers. With these considerations in mind, it can be concluded that the total degrees of freedom required for modeling the out-of-plane displacements in channel section struts is quantified as $3(M+1)(N+1)$.

The presumed polynomial displacement functions within the X and Y directions for both the flanges and web are expressed in Eqs. (9) and (10), respectively:

$$U_w^{ref} = \sum_{p=0}^{P} \sum_{q=0}^{Q} \left(x - \frac{L}{2}\right)\left(x + \frac{L}{2}\right) U_{w,pq}^{ref} x^p y^q$$

$$U_w^{(1)} = U_w^{ref} + \theta_w^{(1)}\left(\frac{h_w^{(1)}}{2}\right)\varphi_{w,x}^{(1)} + \gamma_w^{(1)}\left(\frac{h_w^{(1)}}{2}\right)\psi_{w,x}^{(1)}$$

$$U_w^{(2)} = U_w^{ref} - \theta_w^{(2)}\left(\frac{h_w^{(2)}}{2}\right)\varphi_{w,x}^{(2)} - \gamma_w^{(2)}\left(\frac{h_w^{(2)}}{2}\right)\psi_{w,x}^{(2)}$$

$$\vdots$$

$$U_w^{(n)} = U_w^{(n-1)} - \theta_w^{(n-1)}\left(\frac{h_w^{(n-1)}}{2}\right)\varphi_{w,x}^{(n-1)} - \gamma_w^{(n-1)}\left(\frac{h_w^{(n-1)}}{2}\right)\psi_{w,x}^{(n-1)}$$
$$- \theta_w^{(n)}\left(\frac{h_w^{(n)}}{2}\right)\varphi_{w,x}^{(n)} - \gamma_w^{(n)}\left(\frac{h_w^{(n)}}{2}\right)\psi_{w,x}^{(n)}$$

$$U_{f1}^{ref} = \left[\sum_{p=0}^{P} \sum_{q=0}^{Q} \left(x - \frac{L}{2}\right)\left(x + \frac{L}{2}\right)\left(y' + \frac{b_{f1}}{2}\right) U_{f1,pq}^{ref} x^p y^q\right] + U_w^{ref}\left(x, \frac{b_w}{2}\right)$$

$$U_{f1}^{(1)} = U_{f1}^{ref} + \theta_{f1}^{(1)}\left(\frac{h_{f1}^{(1)}}{2}\right)\varphi_{f1,x}^{(1)} + \gamma_{f1}^{(1)}\left(\frac{h_{f1}^{(1)}}{2}\right)\psi_{f1,x}^{(1)}$$

$$U_{f1}^{(2)} = U_{f1}^{ref} - \theta_{f1}^{(2)}\left(\frac{h_{f1}^{(2)}}{2}\right)\varphi_{f1,x}^{(2)} - \gamma_{f1}^{(2)}\left(\frac{h_{f1}^{(2)}}{2}\right)\psi_{f1,x}^{(2)}$$

$$\vdots$$

$$U_{f1}^{(n)} = U_{f1}^{(n-1)} - \theta_{f1}^{(n-1)}\left(\frac{h_{f1}^{(n-1)}}{2}\right)\varphi_{f1,x}^{(n-1)} - \gamma_{f1}^{(n-1)}\left(\frac{h_{f1}^{(n-1)}}{2}\right)\psi_{f1,x}^{(n-1)}$$
$$- \theta_{f1}^{(n)}\left(\frac{h_{f1}^{(n)}}{2}\right)\varphi_{f1,x}^{(n)} - \gamma_{f1}^{(n)}\left(\frac{h_{f1}^{(n)}}{2}\right)\psi_{f1,x}^{(n)}$$

$$U_{f2}^{ref} = \left[\sum_{p=0}^{P} \sum_{q=0}^{Q} \left(x - \frac{L}{2}\right)\left(x + \frac{L}{2}\right)\left(y'' - \frac{b_{f2}}{2}\right) U_{f2,pq}^{ref} x^p y^q\right] + U_w^{ref}\left(x, \frac{-b_w}{2}\right)$$

$$U_{f2}^{(1)} = U_{f2}^{ref} + \theta_{f2}^{(1)}\left(\frac{h_{f2}^{(1)}}{2}\right)\varphi_{f2,x}^{(1)} + \gamma_{f2}^{(1)}\left(\frac{h_{f2}^{(1)}}{2}\right)\psi_{f2,x}^{(1)}$$

$$U_{f2}^{(2)} = U_{f2}^{ref} - \theta_{f2}^{(2)}\left(\frac{h_{f2}^{(2)}}{2}\right)\varphi_{f2,x}^{(2)} - \gamma_{f2}^{(2)}\left(\frac{h_{f2}^{(2)}}{2}\right)\psi_{f2,x}^{(2)}$$

$$\vdots$$

$$U_{f2}^{(n)} = U_{f2}^{(n-1)} - \theta_{f2}^{(n-1)}\left(\frac{h_{f2}^{(n-1)}}{2}\right)\varphi_{f2,x}^{(n-1)} - \gamma_{f2}^{(n-1)}\left(\frac{h_{f2}^{(n-1)}}{2}\right)\psi_{f2,x}^{(n-1)}$$
$$- \theta_{f2}^{(n)}\left(\frac{h_{f2}^{(n)}}{2}\right)\varphi_{f2,x}^{(n)} - \gamma_{f2}^{(n)}\left(\frac{h_{f2}^{(n)}}{2}\right)\psi_{f2,x}^{(n)} \tag{9}$$

$$V_w^{ref} = \sum_{r=0}^{R} \sum_{s=0}^{S} V_{w,rs}^{ref} x^r y^s$$

$$V_w^{(1)} = V_w^{ref} + \theta_w^{(1)}\left(\frac{h_w^{(1)}}{2}\right)\varphi_{w,y}^{(1)} + \gamma_w^{(1)}\left(\frac{h_w^{(1)}}{2}\right)\psi_{w,y}^{(1)}$$

$$V_w^{(2)} = V_w^{ref} - \theta_w^{(2)}\left(\frac{h_w^{(2)}}{2}\right)\varphi_{w,y}^{(2)} - \gamma_w^{(2)}\left(\frac{h_w^{(2)}}{2}\right)\psi_{w,y}^{(2)}$$

$$\vdots$$

$$V_w^{(n)} = V_w^{(n-1)} - \theta_w^{(n-1)}\left(\frac{h_w^{(n-1)}}{2}\right)\varphi_{w,y}^{(n-1)} - \gamma_w^{(n-1)}\left(\frac{h_w^{(n-1)}}{2}\right)\psi_{w,y}^{(n-1)}$$
$$- \theta_w^{(n)}\left(\frac{h_w^{(n)}}{2}\right)\varphi_{w,y}^{(n)} - \gamma_w^{(n)}\left(\frac{h_w^{(n)}}{2}\right)\psi_{w,y}^{(n)}$$

$$V_{f1}^{ref} = \sum_{r=0}^{R} \sum_{s=0}^{S} V_{f1,pq}^{ref} x^p y^q$$

$$V_{f1}^{(1)} = V_{f1}^{ref} + \theta_{f1}^{(1)}\left(\frac{h_{f1}^{(1)}}{2}\right)\varphi_{f1,y}^{(1)} + \gamma_{f1}^{(1)}\left(\frac{h_{f1}^{(1)}}{2}\right)\psi_{f1,y}^{(1)}$$

$$V_{f1}^{(2)} = V_{f1}^{ref} - \theta_{f1}^{(2)}\left(\frac{h_{f1}^{(2)}}{2}\right)\varphi_{f1,y}^{(2)} - \gamma_{f1}^{(2)}\left(\frac{h_{f1}^{(2)}}{2}\right)\psi_{f1,y}^{(2)}$$

$$\vdots$$

$$V_{f1}^{(n)} = V_{f1}^{(n-1)} - \theta_{f1}^{(n-1)}\left(\frac{h_{f1}^{(n-1)}}{2}\right)\varphi_{f1,y}^{(n-1)} - \gamma_{f1}^{(n-1)}\left(\frac{h_{f1}^{(n-1)}}{2}\right)\psi_{f1,y}^{(n-1)}$$
$$- \theta_{f1}^{(n)}\left(\frac{h_{f1}^{(n)}}{2}\right)\varphi_{f1,y}^{(n)} - \gamma_{f1}^{(n)}\left(\frac{h_{f1}^{(n)}}{2}\right)\psi_{f1,y}^{(n)}$$

$$V_{f2}^{ref} = \sum_{r=0}^{R} \sum_{s=0}^{S} V_{f2,pq}^{ref} x^p y^q$$

$$V_{f2}^{(1)} = V_{f2}^{ref} + \theta_{f2}^{(1)}\left(\frac{h_{f2}^{(1)}}{2}\right)\varphi_{f2,y}^{(1)} + \gamma_{f2}^{(1)}\left(\frac{h_{f2}^{(1)}}{2}\right)\psi_{f2,y}^{(1)}$$

$$V_{f2}^{(2)} = V_{f2}^{ref} - \theta_{f2}^{(2)}\left(\frac{h_{f2}^{(2)}}{2}\right)\varphi_{f2,y}^{(2)} - \gamma_{f2}^{(2)}\left(\frac{h_{f2}^{(2)}}{2}\right)\psi_{f2,y}^{(2)}$$

$$\vdots$$

$$V_{f2}^{(n)} = V_{f2}^{(n-1)} - \theta_{f2}^{(n-1)}\left(\frac{h_{f2}^{(n-1)}}{2}\right)\varphi_{f2,y}^{(n-1)} - \gamma_{f2}^{(n-1)}\left(\frac{h_{f2}^{(n-1)}}{2}\right)\psi_{f2,y}^{(n-1)}$$
$$- \theta_{f2}^{(n)}\left(\frac{h_{f2}^{(n)}}{2}\right)\varphi_{f2,y}^{(n)} - \gamma_{f2}^{(n)}\left(\frac{h_{f2}^{(n)}}{2}\right)\psi_{f2,y}^{(n)} \tag{10}$$

A critical element to consider is the incorporation of reference values, U^{ref} and V^{ref}, representing the in-plane displacements of the flanges and web along the X and Y axes, respectively. These reference values play a pivotal role in ensuring the in-plane continuity condition at the interfaces of the numerical layers, which are discretized across the thickness of each distinct subcomponent, flanges and web. Furthermore, to satisfy the continuity condition at the junction, it is imperative that the reference in-plane displacements of the flange through the X direction (U_f^{ref}) are consistent with those of the web (U_w^{ref}) across the junction at any given length coordinate. It should be noted that $h_f^{(i)}$ and $h_w^{(i)}$ indicate the thickness of the ith numerical layer within the flanges and web, respectively.

Based on the stipulated requirements for continuity and boundary conditions that govern the in-plane displacement functions in both X and Y directions, it is inferable that the total number of degrees of freedom associated with these functions amounts to $3[(P + 1)(Q + 1) + (R + 1)(S + 1)]$.

In addition, the midplane rotation of each numerical layer defined through the flanges and web of the channel section struts with clamped boundary conditions can be expressed as follows with considering the continuity conditions at the junctions. It is also worth noting that the rotational shape functions for channel section struts subject to simply-supported boundary conditions are provided in Appendix B.

$$\varphi_{w,x}^{(1)} = \sum_{j=0}^{J}\sum_{k=0}^{K}\left(x+\frac{L}{2}\right)\left(x+\frac{L}{2}\right)\varnothing_{wx,jk}^{(1)}x^j y^k$$

$$\vdots$$

$$\varphi_{w,x}^{(n)} = \sum_{j=0}^{J}\sum_{k=0}^{K}\left(x+\frac{L}{2}\right)\left(x+\frac{L}{2}\right)\varnothing_{wx,jk}^{(n)}x^j y^k$$

$$\varphi_{f1,x}^{(1)} = \left[\sum_{j=0}^{J}\sum_{k=0}^{K}\left(x+\frac{L}{2}\right)\left(x+\frac{L}{2}\right)\left(y'+\frac{b_{f1}}{2}\right)\varnothing_{f1x,jk}^{(1)}x^j y^k\right] + \varphi_{w,x}^{(1)}\left(x,\frac{b_w}{2}\right)$$

$$\vdots$$

$$\varphi_{f1,x}^{(n)} = \left[\sum_{j=0}^{J}\sum_{k=0}^{K}\left(x+\frac{L}{2}\right)\left(x+\frac{L}{2}\right)\left(y'+\frac{b_{f1}}{2}\right)\varnothing_{f1x,jk}^{(n)}x^j y^k\right] + \varphi_{w,x}^{(n)}\left(x,\frac{b_w}{2}\right)$$

$$\varphi_{f2,x}^{(1)} = \left[\sum_{j=0}^{J}\sum_{k=0}^{K}\left(x+\frac{L}{2}\right)\left(x+\frac{L}{2}\right)\left(y''-\frac{b_f}{2}\right)\varnothing_{f2x,jk}^{(1)}x^j y^k\right]$$
$$+ \varphi_{w,x}^{(1)}\left(x,\frac{-b_w}{2}\right)$$

$$\vdots$$

$$\varphi_{f2,x}^{(n)} = \left[\sum_{j=0}^{J}\sum_{k=0}^{K}\left(x+\frac{L}{2}\right)\left(x+\frac{L}{2}\right)\left(y''-\frac{b_f}{2}\right)\varnothing_{f2x,jk}^{(n)}x^j y^k\right]$$
$$+ \varphi_{w,x}^{(n)}\left(x,\frac{-b_w}{2}\right) \tag{11}$$

$$\varphi_{w,y}^{(1)} = \sum_{d=0}^{D}\sum_{t=0}^{T}\varnothing_{wy,dt}^{(1)}x^d y^t$$

$$\vdots$$

$$\varphi_{w,y}^{(n)} = \sum_{d=0}^{D}\sum_{t=0}^{T}\varnothing_{wy,dt}^{(n)}x^d y^t$$

$$\varphi_{f1,y}^{(1)} = \left[\sum_{d=0}^{D}\sum_{t=0}^{T}\left(y'+\frac{b_{f1}}{2}\right)\varnothing_{f1y,dt}^{(1)}x^d y^t\right] + \varphi_{w,y}^{(1)}\left(x,\frac{b_w}{2}\right)$$

$$\vdots$$

$$\varphi_{f1,y}^{(n)} = \left[\sum_{d=0}^{D}\sum_{t=0}^{T}\left(y'+\frac{b_{f1}}{2}\right)\varnothing_{f1y,dt}^{(n)}x^d y^t\right] + \varphi_{w,y}^{(n)}\left(x,\frac{b_w}{2}\right)$$

$$\varphi_{f2,y}^{(1)} = \left[\sum_{d=0}^{D}\sum_{t=0}^{T}\left(y''-\frac{b_f}{2}\right)\varnothing_{f2y,dt}^{(1)}x^d y^t\right] + \varphi_{w,y}^{(1)}\left(x,\frac{-b_w}{2}\right)$$

$$\vdots$$

$$\varphi_{f2,y}^{(n)} = \left[\sum_{d=0}^{D}\sum_{t=0}^{T}\left(y''-\frac{b_f}{2}\right)\varnothing_{f2y,dt}^{(n)}x^d y^t\right] + \varphi_{w,y}^{(n)}\left(x,\frac{-b_w}{2}\right) \tag{12}$$

Eq. (11) illustrates that the midplane rotation of different numerical layers about the Y-axis, $(\varphi_{w,x}^{(i)},\varphi_{f,x}^{(i)})$, is limited at the longitudinal ends of the channel section strut, $(x = \frac{L}{2}, x = -\frac{L}{2})$. This limitation is a result of the established fixed boundary conditions at these specific edges. Based on the layerwise theory, it is necessary for each numerical layer assumed through the thickness of the flanges and web to possess distinct rotational functions, enhancing the precision in evaluating strain and stress distributions. As illustrated in Fig. 3, the FG-GRC channel section strut is discretized totally into 3n numerical layers, with each layer requiring a distinct rotational shape function. Hence, the cumulative number of unknown coefficients related to these rotational functions is calculated to be $3n\left((J + 1)(K + 1) + (D + 1)(T + 1)\right)$.
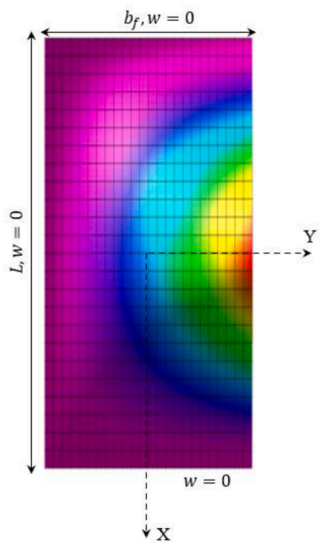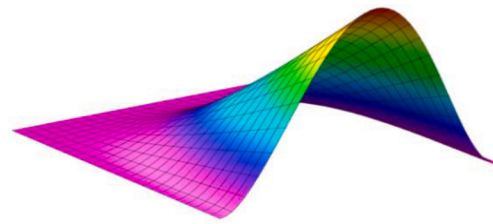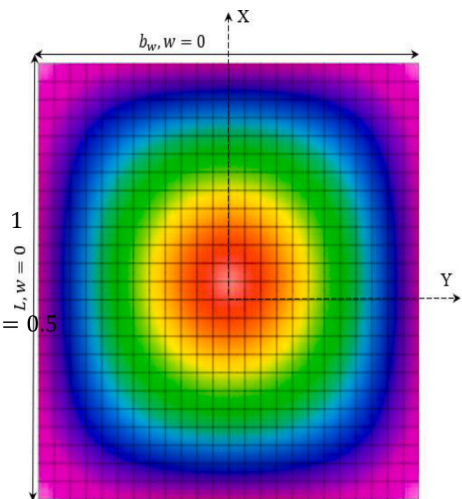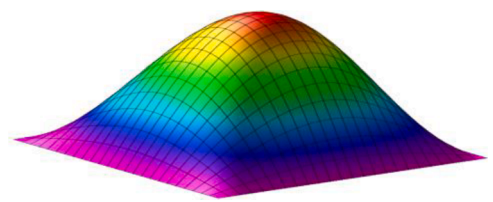
This paper focuses on examining the influence of geometrical imperfections on the nonlinear thermal compressive behavior of channel section struts. These imperfections, which happen due to several reasons including manufacturing tolerances, material defects, thermal effects, and aging, add a realistic dimension to the study. Essentially, these imperfections are deviations from the perfect flatness of FG-GRC laminated channel section struts. Given the boundary conditions and ensuring stress-free edge continuity at the junction, the formulation of the initial imperfection affecting the entire strut is detailed as follows [80]:

$$\overline{W}^* = \eta h sech[\delta_1(x_1 - \psi_1)]cos[\mu_1\pi(x_1 - \psi_1)]sech[\delta_2(x_2 - \psi_2)]cos[\mu_2\pi(x_2 - \psi_2)] \tag{13}$$

where $x_1 = \frac{x+\left(\frac{L}{2}\right)}{L}$ and $x_2 = \frac{y+\left(\frac{b}{2}\right)}{b}$, η is the maximum dimensionless amplitude of the initially deflected geometry, δ_1 and δ_2 are the constants defining the localization degree of the imperfection that is symmetric about ψ_1 and ψ_2 and μ_1 and μ_2 are the half-wave numbers of the imperfection in X and Y-axes, respectively. This equation is designed to accommodate a broad spectrum of initial imperfection patterns.

Table 3 displays the specific geometrical imperfections implemented

Table 3
schematic of local imperfections applied to flange and web of channel section struts.

Segment	Parameters	Imperfection mode (x-y plane)	Imperfection mode (3D)
Flange	$\delta_1 = \delta_2 = 0, \mu_1 = 1, \mu_2 = 0.5$ $\eta = 0.2, \psi_1 = 0.5, \psi_2 = 1$		
Web	$\delta_1 = \delta_2 = 0, \mu_1 = 1, \mu_2 = 1$ $\eta = 0.2, \psi_1 = 0.5, \psi_2 = 0.5$		

locally to the flange and web segments of FG-GRC laminated channel section struts. These imperfections are aligned with the first buckling mode of these thin-walled structures. Highlighting the importance of these imperfections, it is crucial to understand that they play a significant role in the accurate prediction of thermal instability response under various conditions. By simulating real-life scenarios where minor deviations from perfect geometry can have a profound impact on the structural integrity, this method enhances the reliability of structural analysis and design.

In analyzing the nonlinear thermal compressive behavior and the thermally induced pre- and post-buckling free vibration characteristics of FG-GRC laminated channel section struts, the approach is based on the principle of minimum total potential energy. The total potential energy of a structure is a comprehensive measure that encompasses several key components. It includes the potential energy due to external loads, reflecting the work exerted by external forces on the structure. Additionally, it accounts for the total strain energy, which represents the energy associated with internal stresses and deformations within the structure's material. Kinetic energy, which pertains to the motion of the structure, also forms a part of the total potential energy calculation [77]. Regarding the fact that the channel section strut is uniformly subjected to thermal loading, it can be inferred that the potential energy

associated with external forces is negligible. Consequently, in this context, the total potential energy of the structure primarily comprises the sum of its total strain energy and kinetic energy.

Given that the channel section strut's flanges and web are divided into several numerical layers as per layerwise theory, and each layer has specific displacement and rotational functions, the total potential energy of the structure is obtained by summing the strain and kinetic energy of each layer as illustrated in the following equations:

$$\prod^{Total} = \sum_{i=1}^{n} \left(U_w^{(i)} + T_w^{(i)} \right) + \sum_{i=1}^{n} \left(U_{f1}^{(i)} + T_{f1}^{(i)} \right) + \sum_{i=1}^{n} \left(U_{f2}^{(i)} + T_{f2}^{(i)} \right)$$

$$\prod^{Total} = \left(\frac{1}{2}\right) \Bigg[\sum_{i=1}^{n} \int \left(\left(\sigma_w^{(i)}\right)^T \varepsilon_w^{(i)} + \rho h \left(\dot{U}_w^{(i)} + \dot{V}_w^{(i)} + \dot{w}_w^{(i)} \right) \right) dV$$

$$+ \sum_{i=1}^{n} \int \left(\left(\sigma_{f1}^{(i)}\right)^T \varepsilon_{f1}^{(i)} + \rho h \left(\dot{U}_{f1}^{(i)} + \dot{V}_{f1}^{(i)} + \dot{w}_{f1}^{(i)} \right) \right) dV \qquad (14)$$

$$+ \sum_{i=1}^{n} \int \left(\left(\sigma_{f2}^{(i)}\right)^T \varepsilon_{f2}^{(i)} + \rho h \left(\dot{U}_{f2}^{(i)} + \dot{V}_{f2}^{(i)} + \dot{w}_{f2}^{(i)} \right) \right) dV \Bigg]$$

To maintain brevity, the strain and kinetic energy of the first

numerical layer positioned in the web ($U_w^{(1)}$ and $T_w^{(1)}$), illustrated in Fig. 3, are extended in Eqs. (15) and (16), respectively:

$$U_w^{(1)} = \int \frac{1}{2}\, \bar{\sigma}^T \bar{\varepsilon}\, dV$$

$$= \frac{1}{2} \int_{\frac{-b_w}{2}}^{\frac{b_w}{2}} \int_{\frac{-L}{2}}^{\frac{L}{2}} \left(\left\{\varepsilon^0\right\}_w^{(1)} [A]_w^{(1)} \left\{\varepsilon^0\right\}_w^{(1)^T} + 2\left\{\varepsilon^0\right\}_w^{(1)} [B]_w^{(1)} \left\{\varepsilon^1\right\}_w^{(1)^T} \right.$$
$$+ \left\{\varepsilon^1\right\}_w^{(1)} [D]_w^{(1)} \left\{\varepsilon^1\right\}_w^{(1)^T} + 2\left\{\varepsilon^0\right\}_w^{(1)} [E]_w^{(1)} \left\{\varepsilon^3\right\}_w^{(1)^T} + \left\{\varepsilon^1\right\}_w^{(1)} [F]_w^{(1)} \left\{\varepsilon^3\right\}_w^{(1)^T}$$
$$+ \left\{\varepsilon^3\right\}_w^{(1)} [H]_w^{(1)} \left\{\varepsilon^3\right\}_w^{(1)^T} + \left\{\gamma^0\right\}_w^{(1)} [As]_w^{(1)} \left\{\gamma^0\right\}_w^{(1)^T} + 2\left\{\gamma^0\right\}_w^{(1)} [Ds]_w^{(1)} \left\{\gamma^2\right\}_w^{(1)^T}$$
$$\left. + \left\{\gamma^2\right\}_w^{(1)} [Fs]_w^{(1)} \left\{\gamma^2\right\}_w^{(1)^T} \right) \tag{15}$$

$$T_w^{(1)} = \left(\frac{1}{2}\right) \int_{\frac{-b_w}{2}}^{\frac{b_w}{2}} \int_{\frac{-L}{2}}^{\frac{L}{2}} I_w^{(i)} \left[\left(\frac{\partial U_w^{(1)}}{\partial t}\right)^2 + \left(\frac{\partial V_w^{(1)}}{\partial t}\right)^2 + \left(\frac{\partial w_w^{(1)}}{\partial t}\right)^2 \right] dx\, dy = \left(\frac{1}{2}\right)$$

$$\int_{\frac{-b_1}{2}}^{\frac{b_1}{2}} \int_{\frac{-L1}{2}}^{\frac{-L2}{2}} \left[I0_w^{(i)} \left(\frac{\partial U_w^{ref}}{\partial t}\right)^2 + 2I1_w^{(i)}\left(\frac{\partial U_w^{ref}}{\partial t}\frac{\partial \varphi_{w,x}^{(1)}}{\partial t}\right) + I2_w^{(i)}\left(\frac{\partial \varphi_{w,x}^{(1)}}{\partial t}\right)^2 + 2I3_w^{(i)}\left(\frac{\partial U_w^{ref}}{\partial t}\frac{\partial \psi_{w,x}^{(1)}}{\partial t}\right) + 2I4_w^{(i)}\left(\frac{\partial \varphi_{w,x}^{(1)}}{\partial t}\frac{\partial \psi_{w,x}^{(1)}}{\partial t}\right) \right.$$

$$+ I5_w^{(i)}\left(\frac{\partial \psi_{w,x}^{(1)}}{\partial t}\right)^2 + I0_w^{(i)}\left(\frac{\partial V_w^{ref}}{\partial t}\right)^2 + 2I1_w^{(i)}\left(\frac{\partial V_w^{ref}}{\partial t}\frac{\partial \varphi_{w,y}^{(1)}}{\partial t}\right) + I2_w^{(i)}\left(\frac{\partial \varphi_{w,y}^{(1)}}{\partial t}\right)^2$$

$$\left. + 2I3_w^{(i)}\left(\frac{\partial V_w^{ref}}{\partial t}\frac{\partial \psi_{w,y}^{(1)}}{\partial t}\right) + 2I4_w^{(i)}\left(\frac{\partial \varphi_{w,y}^{(1)}}{\partial t}\frac{\partial \psi_{w,y}^{(1)}}{\partial t}\right) I5_w^{(i)}\left(\frac{\partial \psi_{w,y}^{(1)}}{\partial t}\right)^2 + I0_w^{(i)}\left(\frac{\partial w_w^{(1)}}{\partial t}\right)^2 \right] dx\, dy \tag{16}$$

The inertial terms are obtained through the integration of the density.

$$\left\{ I_0^{ij} \quad I_1^{ij} \quad I_2^{ij} \quad I_3^{ij} \quad I_4^{ij} \quad I_5^{ij} \right\} = \int_{-\frac{h^{ij}}{2}}^{\frac{h^{ij}}{2}} \rho(z)\left\{ 1 \quad \theta_1(z) \quad \theta_1^2(z) \quad \theta_2(z) \quad \theta_1(z)\theta_2(z) \quad \theta_2^2(z) \right\} dz \tag{17}$$

Following this stage, the total potential energy should be minimized by using the unknown displacement and rotation coefficients as shown in Eqs. (18) and (19) [81]

$$\frac{\partial \prod}{\partial \chi} = 0 \tag{18}$$

where χ is the vector of unknowns, expressed by

$$\left\{ \sum_{p=0}^{P}\sum_{q=0}^{Q}\left(u_{w,pq}^{ref} + u_{f1,pq}^{ref} + u_{f2,pq}^{ref}\right), \sum_{r=0}^{R}\sum_{s=0}^{S}\left(v_{w,rs}^{ref} + v_{f1,rs}^{ref} + v_{f2,rs}^{ref}\right), \sum_{m=0}^{M} \right.$$
$$\times \sum_{n=0}^{N}\left(w_{w,mn}^{ref} + w_{f1,mn}^{ref} + w_{f2,mn}^{ref}\right), \left(\sum_{i=1}^{n}\sum_{j=0}^{J}\sum_{k=0}^{K}\varnothing_{wx,jk}^{(i)} + \sum_{i=1}^{n}\sum_{j=0}^{J}\right.$$
$$\times \sum_{k=0}^{K}\varnothing_{f1x,jk}^{(i)} + \sum_{i=1}^{n}\sum_{j=0}^{J}\sum_{k=0}^{K}\varnothing_{f2x,jk}^{(i)}\right), \left(\sum_{i=1}^{n}\sum_{d=0}^{D}\sum_{t=0}^{T}\varnothing_{wy,dt}^{(i)} + \sum_{i=1}^{n}\sum_{d=0}^{D}\right.$$
$$\left. \times \sum_{t=0}^{T}\varnothing_{f1y,dt}^{(i)} + \sum_{i=1}^{n}\sum_{d=0}^{D}\sum_{t=0}^{T}\varnothing_{f2y,dt}^{(i)} \right\} \tag{19}$$

Eq. (18) leads to the nonlinear general dynamic matrix equation of the FG-GRC channel section strut:

$$[\boldsymbol{M}]\{\ddot{\boldsymbol{\chi}}\} + [\boldsymbol{K}(\boldsymbol{T},\boldsymbol{\chi})]\{\boldsymbol{\chi}\} = \{\boldsymbol{F}(\boldsymbol{T})\} \tag{20}$$

Where $[\boldsymbol{M}]$ is the mass matrix, $[\boldsymbol{K}(\boldsymbol{T},\boldsymbol{\chi})]$ is the stiffness matrix; $\{\ddot{\boldsymbol{\chi}}\}$ and $\{\boldsymbol{\chi}\}$ are the Jacobi expanded coefficients, and {F(T)} is the force matrices.

To solve Eq. (20), it can be assumed that

$$\chi = \chi_s + \chi_t \tag{21}$$

Where χ_s is the time-independent particular solution which means the incremental thermal large deflection, and χ_t is the time-dependent. Therefore, by substituting Eq. (21) into Eq. (20), two sets of system of equations can be obtained as:

$$[\boldsymbol{K}(\boldsymbol{T},\boldsymbol{\chi})]\{\boldsymbol{\chi}_s\} = \{\boldsymbol{F}(\boldsymbol{T})\} \tag{22}$$
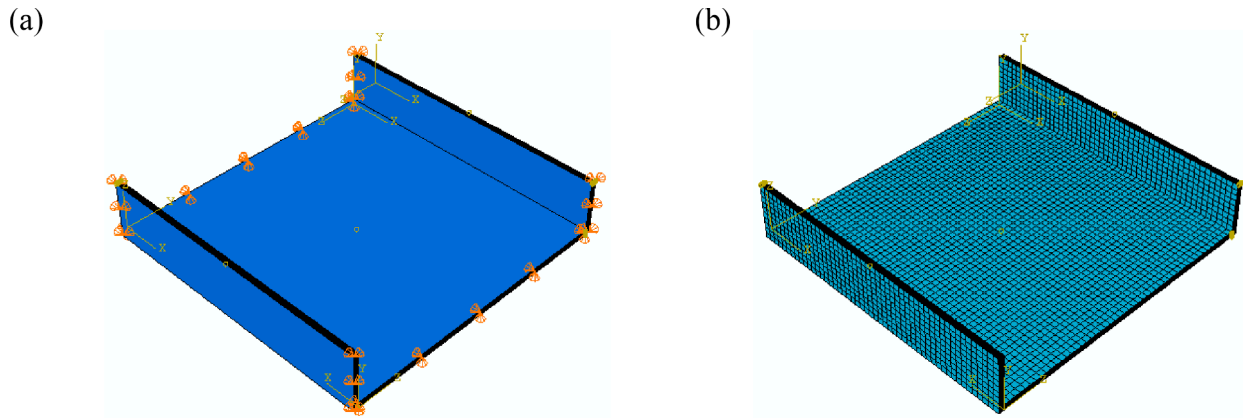
(a)

(b)

Fig. 4. A typical channel section strut modelled based on the finite element simulation (a) implementing clamped boundary conditions, (b) diagrammatic representation of the mesh for the channel section strut.

$$[\boldsymbol{M}]\{\ddot{\chi}_t\} + [\boldsymbol{K}(\boldsymbol{T},\chi)]\{\chi_t\} = 0 \qquad (23)$$

Eq. (22) addresses the nonlinear thermal post-buckling analysis, while Eq. (23) is formulated for examining the thermally induced vibrations in channel section struts. In addition, the subscripts 's' and 't' denote the static and dynamic displacement of the plate, respectively. The Newton-Raphson iterative method is frequently employed to solve nonlinear systems of equations in thermal post-buckling analysis, Eq. (22). After resolving the Eq. (22) and determining the displacement for the given thermal load, it is essential to refresh and incorporate the tangent stiffness matrix, $[\boldsymbol{K}(\boldsymbol{T},\chi)]$, into Eq. (23). This step facilitates solving the eigenvalue equation, thereby enabling the computation of linear fundamental frequencies.

3.2. Modelling based on the finite element simulation

To validate the accuracy of the results derived from the LW-TSDT approach, this study employs a sophisticated 3D-FEM developed using the ABAQUS, which encompasses two critical phases. Initially, a comprehensive 3D model is constructed, integrating specific material characteristics, load conditions, and boundary parameters. Subsequently, a linear perturbation buckling analysis is conducted to identify the various buckling modes of the channel section struts. Following this, the analysis transitions to the static Riks method, replacing the linear buckling approach. This method considers nonlinear geometric factors, incorporating the first buckling mode shape identified earlier as an imperfection within the Riks method. It's imperative to highlight the significant impact of the imperfection amplitude on the convergence of the nonlinear post-buckling analysis. In the nonlinear simulation conducted using ABAQUS, the imperfection amplitude for the channel section struts is set to 0.001 times the magnitude of the initial buckling mode shape.

In this research, as previously highlighted, the edge supports are modeled as either clamped or simply-supported boundary conditions. Additionally, it is crucial to consider that the in-plane displacement of the channel section struts in the X direction must be constrained, as illustrated in Fig. 4(a). This constraint is particularly pertinent due to the

Table 5
The efficiency parameters η_i, $i = 1, 2, 3$ for different volume fractions of graphene sheets at three different levels of temperature [30,31,34].

T (K)	V_G	η_1	η_2	η_3
300	0.03	2.929	2.855	11.842
	0.05	3.068	2.962	15.944
	0.07	3.013	2.966	23.575
	0.09	2.647	2.609	32.816
	0.11	2.311	2.260	33.125
400	0.03	2.977	2.896	13.928
	0.05	3.128	3.023	15.229
	0.07	3.060	3.027	22.588
	0.09	2.701	2.603	28.896
	0.11	2.405	2.337	29.527
500	0.03	3.388	3.382	16.712
	0.05	3.544	3.414	16.018
	0.07	3.462	3.339	23.428
	0.09	3.058	2.936	29.754
	0.11	2.736	2.665	30.773

thermal loading involved in the study. When the temperature uniformly increases, it induces expansion throughout the entire structure. The imposed restriction counteracts this expansion, thereby precipitating the buckling phenomenon.

In the finite element simulation, the 3D, 8-node, linear isoperimetric element (C3D8) is utilized. The C3D8 element in ABAQUS represents a brick-shaped volume with eight nodes situated at specific coordinates in the 3D space, defining its geometry. It is capable of deformation and shape alteration when subjected to applied loads or constraints. With each node having three DOFs, translation displacement along the X, Y, and Z axes, the element possesses a total of 24 DOFs (8 nodes * 3 DOFs per node).

4. Results and discussion

The nonlinear compressive instability of composite laminated channel section struts reinforced by graphene sheets is investigated using the approach described in the preceding sections. For the matrix,

Table 4
. Thermomechanical properties of single layer graphene sheet with geometrical characteristics $\boldsymbol{a}^G = 14.76$ $\boldsymbol{nm}$, $\boldsymbol{b}^G = 14.77$ $\boldsymbol{nm}$, $\boldsymbol{h}^G = 0.188$ $\boldsymbol{nm}$ [75].

T [K]	E_{11}^G[TPa]	E_{22}^G[TPa]	G_{12}^G[TPa]	ν_{12}^G	α_{11}^G [10^{-6}/K]	α_{22}^G [10^{-6}/K]
300	1.812	1.807	0.683	0.177	−0.9	−0.95
400	1.769	1.763	0.691	0.177	−0.35	−0.4
500	1.748	1.735	0.700	0.177	−0.08	−0.08
700	1.737	1.721	0.676	0.177	0.25	0.3
1000	1.660	1.646	0.645	0.177	0.32	0.32

Poly (methyl methacrylate), also known as PMMA, is chosen, and it is characterized by material properties $E^m = (3.52 - 0.0034T)$GPa, $\nu^m = 0.34$, and $\alpha^m = 45 \times 10^{-6}(1 + 0.0005(T - T_0))K^{-1}$ [75]. Additionally, the reinforcement for each layer consists of graphene sheets with an effective thickness of $h^G = 0.188$ nm. Due to the pronounced influence of temperature variation on graphene sheets' material properties, an MD simulation was employed by Lin et al. [75] to derive the material characteristics of graphene sheets at different temperatures, as depicted in Table 4.

The extended Halpin-Tsai approach, as presented in Eq. (1), was introduced to enhance the precision of material property determination for GRC laminated channel section struts, which builds upon the original
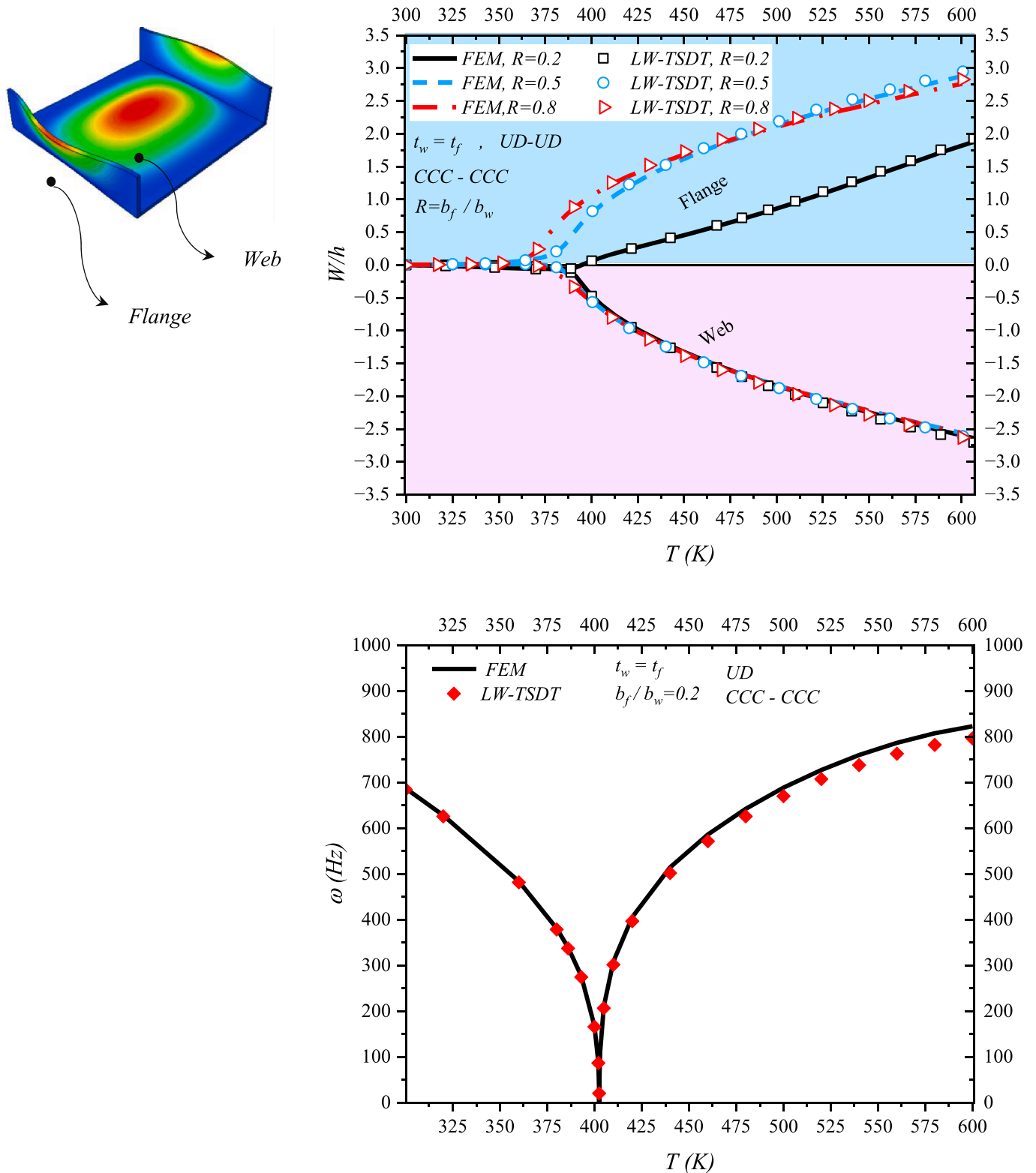

Fig. 5. Comparison the results obtained from FEM and LW-TSDT (a) nonlinear thermal equilibrium paths of flange and web in a channel section strut (b) variations in pre-and post-buckling fundamental frequencies.

Halpin-Tsai method. This approach involves several efficiency parameters denoted as η_i, where i takes the values of 1, 2, and 3. The evaluation of these parameters for five different graphene volume fractions at three different temperatures was conducted by Shen et al. [30,31,34], and the results are shown in Table 5.

In all cases studied in this work, the specified GRC laminated channel section struts (flanges and web) consist of ten plies stacked in the sequence $[0, 90, 0, 90, 0]_s$. As mentioned, the investigation involves the utilization of seven distinct graphene distributions to reinforce the specified composite channel section strut. Among these distributions, one is the UD pattern, while the remaining six follow a functionally graded distribution. Moreover, it should be emphasized that in this study, the thicknesses of both the web and flanges are maintained identical, $(t_f = t_w)$.

4.1. GRC laminated channel section strut with UD graphene pattern

One of the principal targets of this study is to undertake a comprehensive comparative evaluation of how varying graphene distribution patterns impact the nonlinear thermal instability responses and the thermally induced natural frequencies variations in composite laminated channel section struts, both in pre-buckling and post-buckling states. To achieve this objective, a thorough comparison is made between several graphene distribution patterns, with the UD pattern serving as the reference case.

The comparison methodology employed in this research comprises three distinct phases. initially, the comparative analysis begins with the presumption that each distinct segment of the channel section strut, which includes two vertical walls (flanges) and one horizontal wall (web), is constructed from ten plies of graphene reinforced composite material, all adhering to the UD distribution pattern. Following this assumption, a detailed nonlinear thermal instability analysis is performed to acquire results pertinent to the reference case. In the second step of the comparative analysis, the graphene distribution patterns through the flanges thickness are altered to include various non-uniform distribution patterns such as FG-X, FGX-FGX, FG-O, FGO-FGO, FG-V, and FGV-FGV. This analysis endeavors to ascertain which specific types of non-uniform graphene distribution patterns, applied through the flanges, exert the most and least significant impact on the critical buckling temperature and fundamental natural frequencies of the channel section struts, while maintaining a constant UD graphene distribution pattern across the web's thickness in all case studies.

The final step involves selecting and maintaining the best non-uniform graphene distribution pattern for the flanges obtained from the second steSimultaneously, the web is subjected to a variety of non-uniform graphene distribution patterns, replacing the initial UD pattern. Consequently, it becomes feasible to identify the optimal combination of graphene distribution patterns that can be applied across the thickness of the flanges and web, with the aim of improving the critical buckling temperature and fundamental natural frequencies. Furthermore, this process is conducted again, but this time employing the least effective non-uniform graphene distribution patterns for the flanges. The purpose of this stage is to conclusively recognize the least efficient combination of graphene distribution patterns when used on the entire channel section strut.

Two key points should be highlighted for clarity: First, in all the scenarios examined in this paper, the graphene distribution pattern is kept identical for both flanges to ensure symmetry. Second, the total volume percentage of graphene used remains the same in all case studies; the primary difference lies in the distribution patterns of the graphene.

Prior to initiating the comparative analysis of various graphene distribution patterns using the aforementioned methodology, it's crucial to establish a baseline of verification results. Fig. 5(a) showcases the thermal equilibrium paths for channel section struts with three different

Table 6

Comparison of computing time and CPU usage in performed simulations and computational performance of proposed methodology (UD, $b_f/b_w = 0.2$, $t_f/t_w = 1$, CCC—CCC).

Solution method		
Present Method	DOF	6591
(LW-TSDT)	Running time (s)	938
	CPU usage (%)	25 %
Finite Element Method	DOF	17,421
(ABAQUS)	Running time (s)	1247
	CPU usage (%)	37 %
Discrepancy performance time (%)		33%
$\frac{(ABAQUS - LWTSDT)}{LWTSDT} \times 100$		

shape factors, $\boldsymbol{R} = \boldsymbol{b_f}/\boldsymbol{b_w}$, reinforced with a UD graphene distribution pattern and considering the clamped boundary conditions at both longitudinal ends of the structure. Additionally, Fig. 5(b) confirms the changes in the fundamental frequency of the plate both in pre-and post-buckling conditions.

This paper employs a specific notation to represent boundary conditions: 'CCC—CCC' for clamped and 'SSS-SSS' for simply-supported conditions. This format reflects the setup where, at each longitudinal end of the structure, there are three edges, two belonging to the flanges and one to the web's edge. The notation confirms that at both ends, all edges are subjected to the same type of boundary condition. Moreover, the various types of graphene reinforcement combinations utilized for the web and flanges of the channel section struts, represented schematically in the A-B format. In this notation, the first element (A) represents the graphene distribution pattern applied to the web, and the second element (B) corresponds to the specific type of graphene reinforcement pattern used for the flange. For example, in the UD-FGX case, UD refers to the graphene distribution for the web, and FGX indicates the graphene distribution pattern adopted for the flanges in the channel section struts.

As shown, the deflection curve for the flange corresponds to the center of its longitudinal free edge, while the deflection of the web is associated with its central point. These paths are derived using the LW-TSDT and compared with outcomes from numerical simulations conducted using the ABAQUS commercial software.

A preliminary analysis of Fig. 5 reveals a significant correlation between the findings acquired from the LW-TSDT and those computed using the FEM. Moreover, the results demonstrate that increasing the flange width dimension inversely affects the compressive strength of the channel section struts, leading to greater flange deflection in the post-buckling phase and a subsequent decrease in the critical buckling temperature. To clarify, with a flange-to-web width ratio $\boldsymbol{R} = 0.2$, the critical buckling temperature for UD channel section struts is approximately $\boldsymbol{T} = 400\ \boldsymbol{K}$. Increasing this ratio to $\boldsymbol{R} = 0.8$ results in a reduction of the critical buckling temperature to $\boldsymbol{T} = 370\ \boldsymbol{K}$. Another interesting observation that can be drawn from the figure is the apparent lack of noticeable influence of varying flange widths on the post-buckling equilibrium path of the web. This is evidenced by the nearly identical web post-buckling deflection across three different shape factor types.

Furthermore, there is a strong correlation between the results derived from FEM and those obtained through LW-TSDT regarding the pre-and post-buckling analysis of channel section struts. These struts are characterized by clamped boundary conditions and are reinforced with a UD graphene distribution pattern.

The LW-TSDT approach accounts for 6591 degrees of freedom (DOFs) in its buckling analysis for the UD laminated composite channel section strut, which is reflected in a stiffness matrix of the order 6591 by 6591. On the other hand, the finite element analysis utilizes 3D 8-node linear hexahedral elements (C3D8), resulting in a total of 17,421 DOFs. This marked discrepancy in the DOFs between the semi-analytical LW-TSDT and the numerical finite element method underscores the
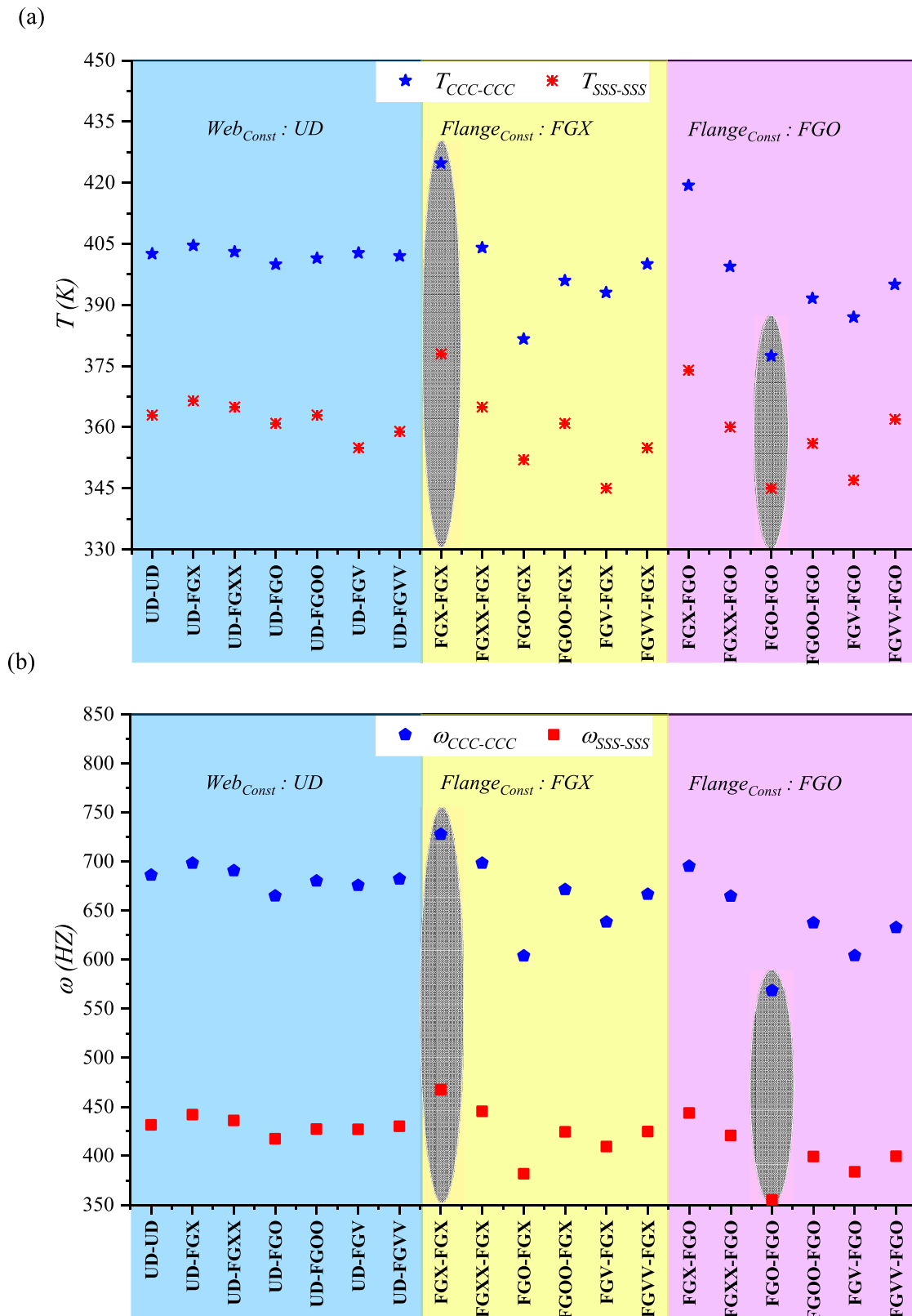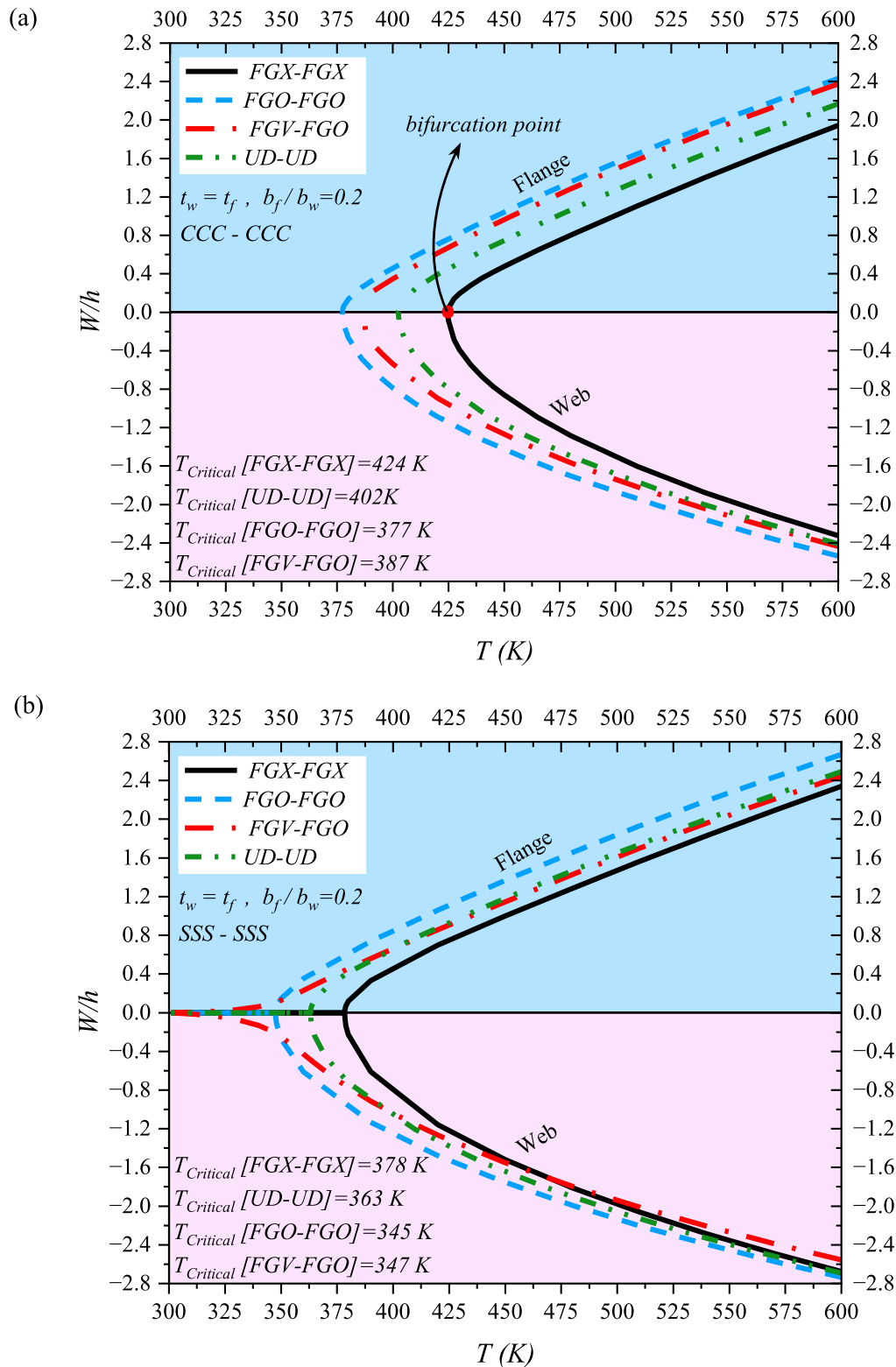
(a)

(b)

Fig. 6. Investigation the influence of various kinds of graphene distribution patterns and boundary conditions on the critical buckling temperatures and fundamental natural frequencies of laminated channel section struts.

Fig. 7. Investigation the boundary conditions and various graphene distribution patterns on the thermal equilibrium paths of laminated channel section struts subjected to uniform temperature rise (a) clamped (b) simply-supported.

enhanced computational efficiency of the LW-TSDT. Table 6 offers a detailed summary of the analysis in terms of runtime and CPU usage. A cursory review of this table clearly shows that the implemented LW-TSDT method operates around 33 % faster in terms of runtime compared to the numerical finite element simulation.

4.2. Influence of different graphene distribution patterns on the post-buckling equilibrium paths and vibration characteristics of channel section struts

By conducting a nonlinear thermal instability analysis of polymeric laminated channel section struts, reinforced with various graphene

distribution patterns, and subjected to both clamped and simply-supported boundary conditions, Fig. 6 compares the outcomes pertaining to their critical buckling temperatures and fundamental natural frequencies. Following the aforementioned explanations, the initial step of the comparison involves case studies, where UD graphene distribution pattern is consistently applied across the web, while variations in

graphene dispersions are examined in the thickness direction of the flanges. The outcomes of these studies are presented in Figs. 6(a) and (b), distinguished by a blue background for clarity. The results demonstrate that where the web is reinforced with UD graphene distribution, the configuration employing FGX graphene distribution for flanges reinforcement yield the highest critical buckling temperatures and
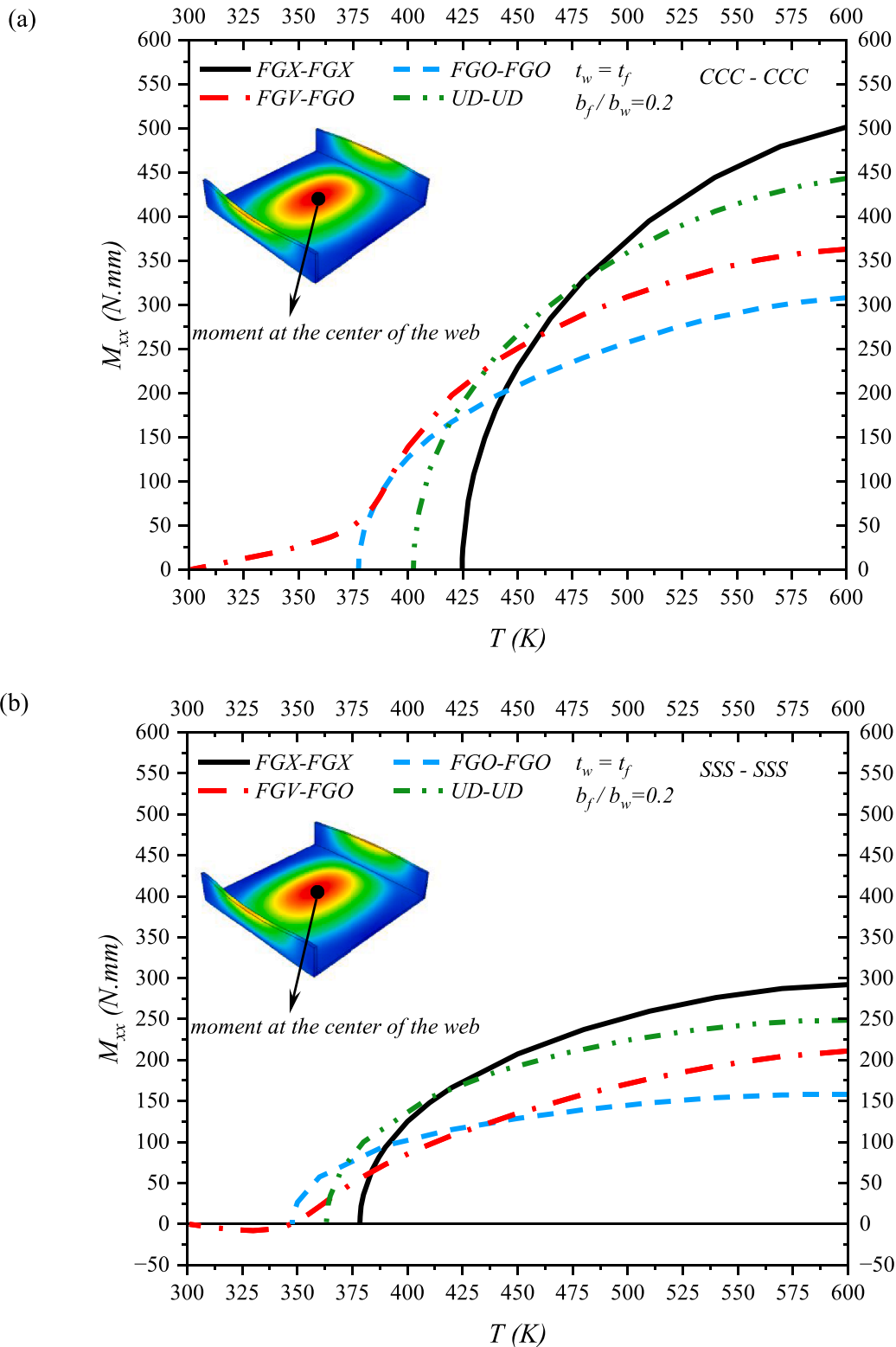

Fig. 8. Influence the boundary conditions and various graphene distribution patterns on the variation of bending moment at the center of the web (a) clamped (b) simply-supported.

fundamental natural frequencies. Conversely, configuration with FGO graphene distribution in the flanges are associated with the lowest values for both critical buckling temperature and fundamental natural frequency.

In the subsequent step of the comparative analysis, the FGX graphene

distribution pattern, identified as the most effective, is consistently applied for reinforcing the flanges. Concurrently, various non-uniform graphene dispersions are explored through the thickness direction of the web. The results pertaining to this specific scenario are demonstrated within the yellow regions of Figs. 6(a) and (b). The findings

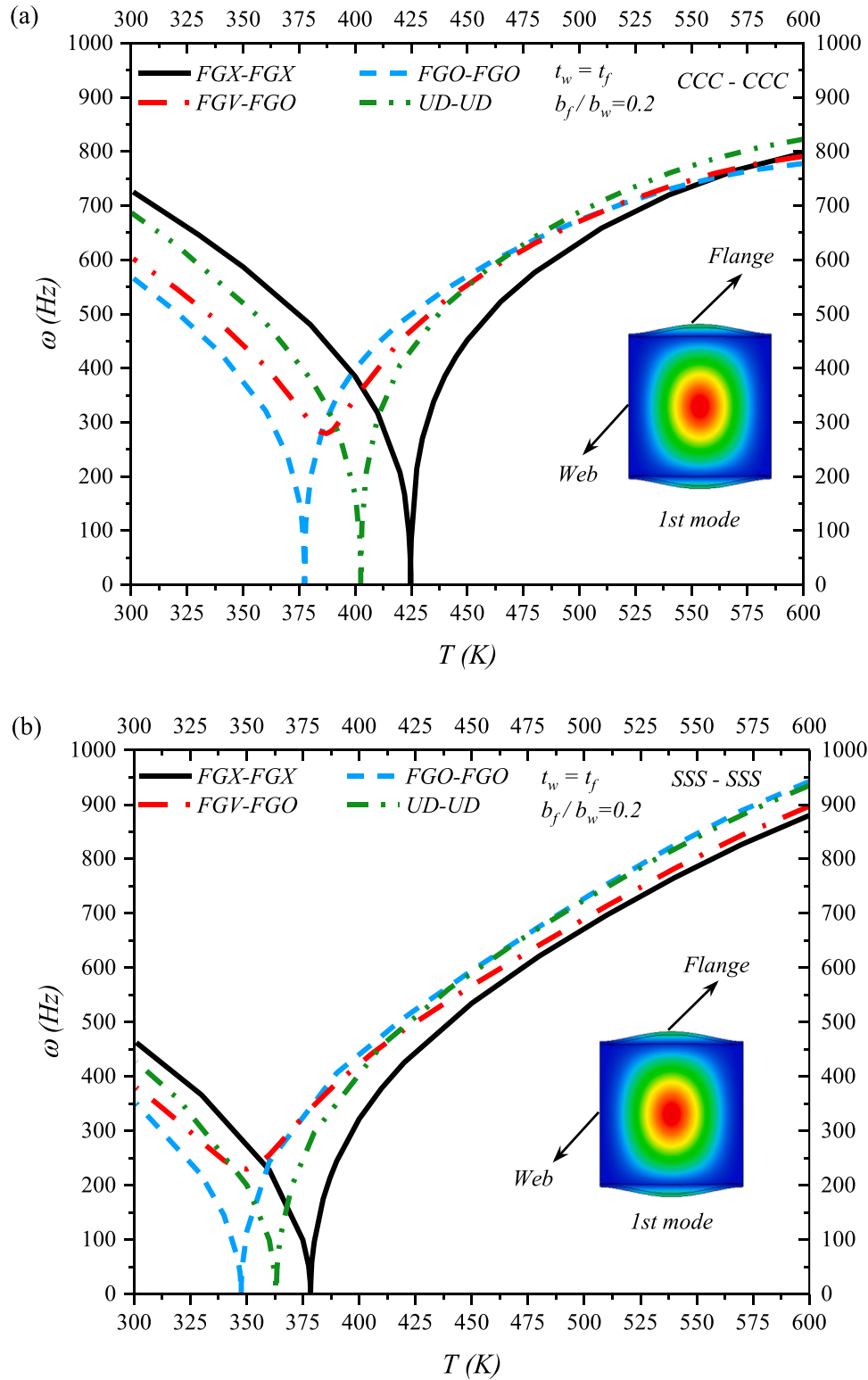**Fig. 9.** Influence of different graphene distribution patterns on variations of thermally induced pre- and post-buckling of laminated channel section struts (a) fundamental frequency with clamped boundary condition (b) fundamental frequency with simply-supported boundary condition (c) second mode frequency with clamped boundary condition (d) second order with simply-supported boundary condition.
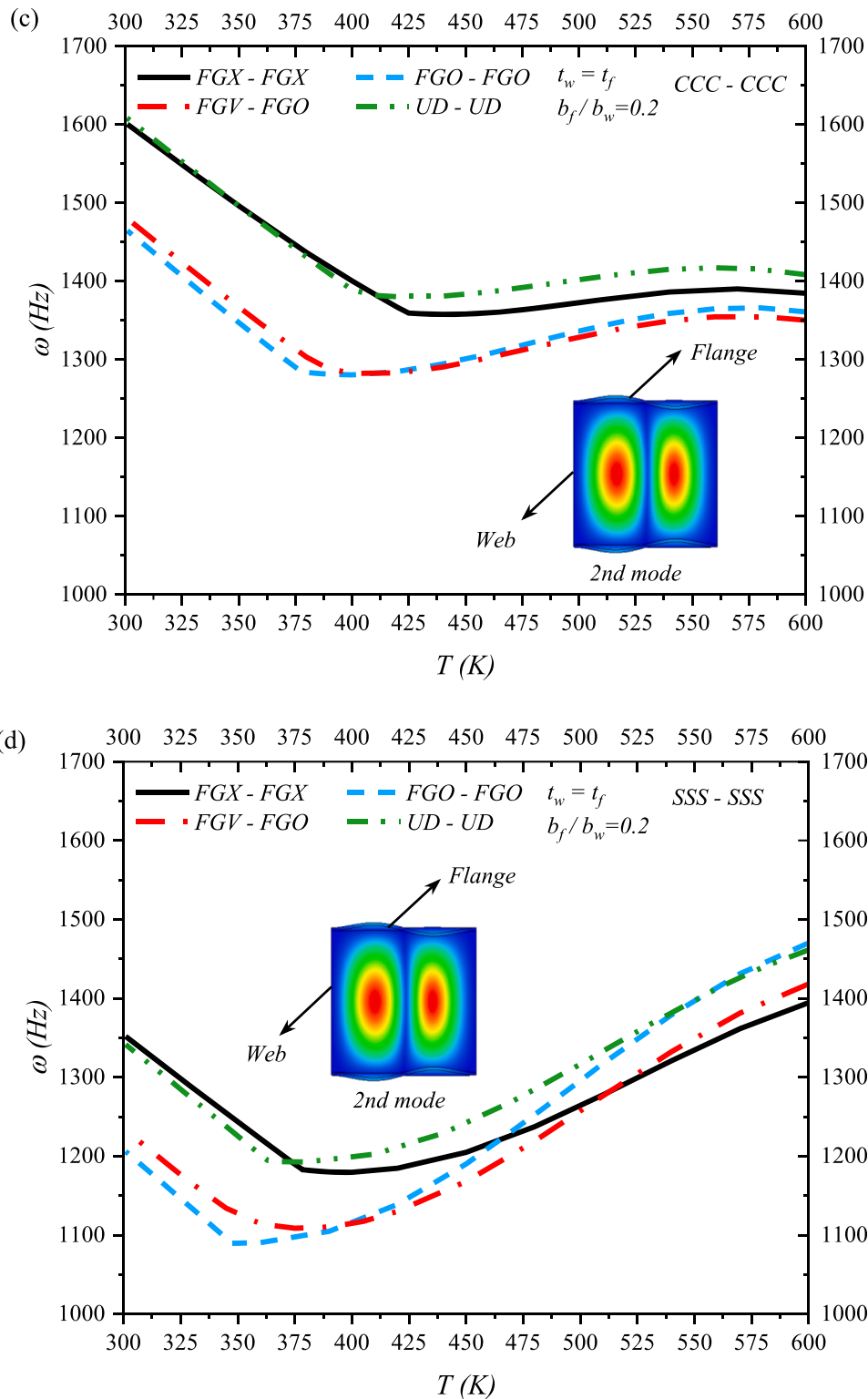
Fig. 9. (*continued*).

confirm that when the FGX graphene distribution pattern is employed for both the flanges and the web, the laminated channel section struts achieve their peak performance in terms of critical buckling temperature and fundamental natural frequency.

Furthermore, this scenario is replicated with the objective of identifying the least effective graphene distribution pattern. This is illustrated in the pink area of Fig. 6. Here, the FGO graphene distribution, acknowledged as the least effective, is selected for reinforcing the flanges of the channel section struts. simultaneously, a range of non-uniform graphene distributions are explored through the thickness direction of the web. The results conclusively demonstrate that the lowest critical buckling temperature and fundamental natural frequency correspond to the case in which both the flanges and the web are reinforced with the FGO graphene distribution pattern.

Based on the findings presented in Fig. 6, the subsequent section of this paper will undertake a comparative analysis of four distinct
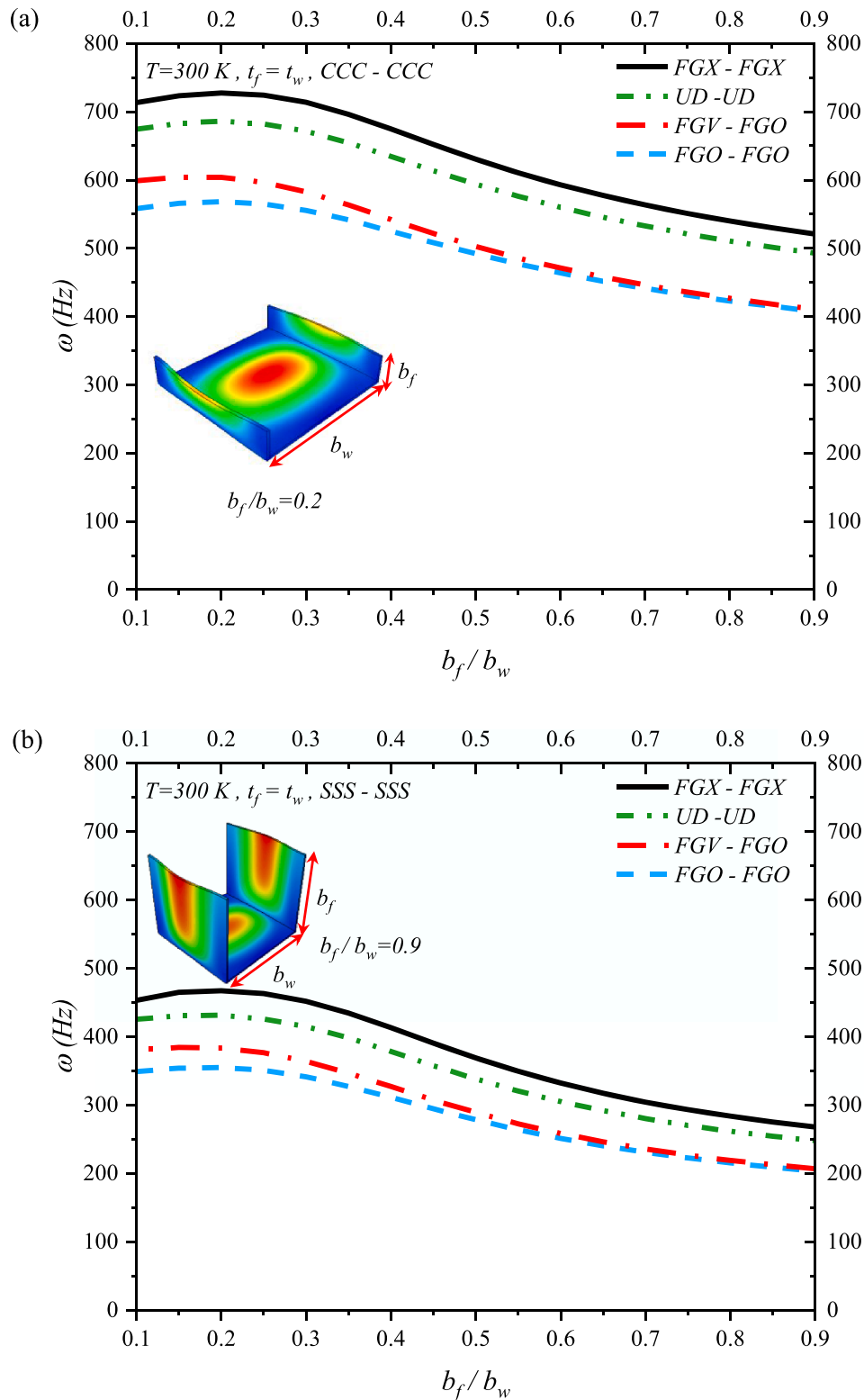
Fig. 10. Influence of various graphene distribution patterns and geometrical parameters on the fundamental frequencies of FG-GRC channel section struts (a) clamped boundary condition (b) simply-supported boundary condition.

graphene distribution patterns. These patterns will be evaluated from various analytical perspectives, including thermal post-buckling equilibrium paths, bending moment, and pre- and post-buckling thermally induced free vibration. It is important to note that the four graphene

patterns under review include UD-UD, serving as the benchmark case, along with FGX-FGX and FGO-FGO, identified respectively as the most and least effective scenarios. Additionally, the analysis will also consider the FGV-FGO combination, where an asymmetric graphene distribution

pattern (FGV) is utilized for reinforcing the web.

Fig. 7 presents a comparison of the thermal post-buckling equilibrium paths for laminated channel section struts, reinforced with various uniform and non-uniform graphene distribution patterns. As depicted, Fig. 7(a) pertains to the struts under clamped (CCC—CCC) boundary conditions, whereas Fig. 7(b) displays the outcomes for struts with simply-supported (SSS-SSS) boundary conditions. The results clearly demonstrate that, under both types of boundary conditions, laminated channel section struts reinforced with FGX graphene distribution pattern exhibit a higher critical buckling temperature compared to those with alternative graphene dispersions. Furthermore, during the post-buckling phase, the deflection observed at the flange (center of the free edge) and the web (central point) is comparatively lower in the FGX graphene reinforced cases than in other graphene distribution patterns. Conversely, independent of the boundary conditions applied, structures reinforced with FGO graphene distribution pattern experience a lower critical buckling temperature and a higher post-buckling deflection at the flange and web. For example, consider a scenario with a clamped boundary condition where the geometrical parameters of the channel section strut, and the total percentage of graphene utilized in reinforcing the laminated structure remain constant. Adjusting the graphene distribution pattern from FGO to FGX results in a relative increase of 12 % in the critical buckling temperature.

From Fig. 7, another significant observation emerges regarding the distinctive thermal equilibrium path of the FGV-FGO laminated channel section strut under simply-supported boundary conditions. This path markedly differs from those associated with other graphene distribution patterns that preserve symmetry or those found in channel section struts subjected to clamped boundary conditions.

The results illustrate that in cases featuring symmetric graphene distribution patterns, the thermal equilibrium paths exhibit a primary-secondary characteristic. The stable primary thermal equilibrium path is defined by a direct correlation between the applied thermal load and the structural response. As illustrated in Fig. 7, up until the critical buckling temperature, identified as the point of instability or bifurcation, both flanges and the web retain a flat configuration with no out-of-plane displacement, signifying their alignment with the primary equilibrium path. At the onset of the critical buckling temperature, however, there is a noticeable jump in the deflection of both the flanges and the web. Consequently, in the post-buckling state, the instability response of both the flanges and the web is characterized by their transition to the second set of equilibrium paths.

Nonetheless, the thermal equilibrium path exhibited by simply-supported channel section struts reinforced with FGV-FGO graphene distribution patterns is distinct. Initially, as thermal loading commences, the structure undergoes out-of-plane displacement, transitioning into the first buckling mode shape. However, the magnitude of this initial deflection is minimal. Notably, the rate of deflection increases near specific temperatures, $T = 347$ K. The observed phenomenon is due to the generation of non-zero thermal bending moments within the web reinforced with FGV graphene distribution pattern under thermal loading. This arises from stretching-bending coupling of asymmetric graphene distribution pattern, a process clearly illustrated in Fig. 8.

Fig. 8 demonstrates that under both clamped and simply-supported boundary conditions, the bending moment at the center of the web, reinforced with symmetric graphene distribution patterns, remains zero until the critical buckling temperature. At this point, a bending moment is induced, leading to deflection. In contrast, for the web reinforced with FGV, characterized as an asymmetric graphene distribution pattern, a bending moment is present at the center of the web from the initial stage of thermal loading. The rate of change in this bending moment intensifies around $T = 387$ K for clamped boundary conditions and $T = 347$ K for simply-supported conditions. It should be noted that the simply-supported edge lacks the capability to provide an additional moment necessary for maintaining the flatness of the channel section strut, in contrast to a clamped structure, where the supports are designed to exert an extra moment.

Fig. 9 illustrates the variation of thermally induced pre- and post-buckling vibration of FG-GRC channel section struts. At the reference temperature, both the fundamental and second order natural frequencies of FGX channel section struts are higher compared to those reinforced with other types of graphene distribution patterns.

As indicated, independent of the variations in graphene distribution patterns and boundary conditions, a uniform increase in temperature leads to a continuous decrease in both the first and second-order natural frequencies during the pre-buckling phase. This decrease continues until reaching near the critical buckling temperature or instability point, primarily because of the reduction in stiffness caused by in-plane compressive thermal loading. It is essential to highlight that, across the majority of the cases examined, following the critical buckling temperature in the post-buckling phase, there is an observed increase in both first second natural frequencies. This perception emphasizes the predominance of the stiffening effect because of static buckling deformation over the softening impact induced by thermal stress.

In the analysis of fundamental natural frequencies, it is observed that, in instances where symmetric graphene distribution patterns (FGX, FGO, UD) reinforce the laminated channel section strut, these fundamental frequencies diminish to zero at the critical buckling temperature, before transitioning into the post-buckling phase. Conversely, Employing an asymmetric graphene distribution pattern (FGV) results in an elevation of the fundamental frequency close to the critical buckling temperature. This approach prevents the frequency from decreasing to zero. The underlying mechanism involves the generation of thermal bending moment through the web at the beginning stage of thermal loading, as discussed in Fig. 8. This bending moment induces static buckling deflection, which, as noted, leads to an increase in stiffness.

As mentioned, FGX channel section struts exhibit enhanced thermal compressive strength relative to alternative configurations, causing them to transition into the post-buckling phase at a later stage compared to other cases. Consequently, the fundamental natural frequencies during the post-buckling phase are lower for FGX struts than for structures reinforced with other types of graphene distribution patterns.

An additional insight derived from Fig. 9 pertains to the variance in the fundamental and second-order natural frequencies under different boundary conditions. Specifically, in the pre-buckling stage, the fundamental frequencies of channel section struts with clamped boundary conditions are substantially higher than those with simply-supported boundary conditions. Conversely, this pattern reverses in certain segments of the post-buckling phase, indicating a notable shift in frequencies behavior dependent on the boundary condition applied. For example, at the reference temperature of $T = 300$ K, the fundamental frequency of FGX channel section struts under clamped boundary conditions is approximately 1.67 times greater than that of struts with simply-supported boundary conditions. However, at the maximum temperature of $T = 600$ K in the post-buckling phase, this ratio decreases to 0.9.

Investigation the influence of the shape factor of channel section struts (b_f/b_w), which is the ratio of the flange width to the web width, on their fundamental natural frequencies at the reference temperature ($T = 300$ K) is conducted in Fig. 10. As with the earlier results, this analysis is undertaken for both clamped and simply-supported boundary conditions. A key inference drawn from these findings is that, irrespective of the boundary condition type, an increase in the shape factor, assuming a constant web width while the flange width increases, leads to a decrease in the fundamental natural frequencies. This suggests a significant reduction in the compressive stiffness of the structure. This phenomenon can be logically attributed to the increased leverage effect of the wider flanges, which amplifies bending and reduces the overall stiffness, thereby impacting the fundamental frequency characteristics.

Furthermore, the optimal shape factor for laminated channel section struts, as suggested by the data, is approximately $b_f/b_w = 0.2$, where the structure exhibits the highest fundamental frequencies. Specifically, in
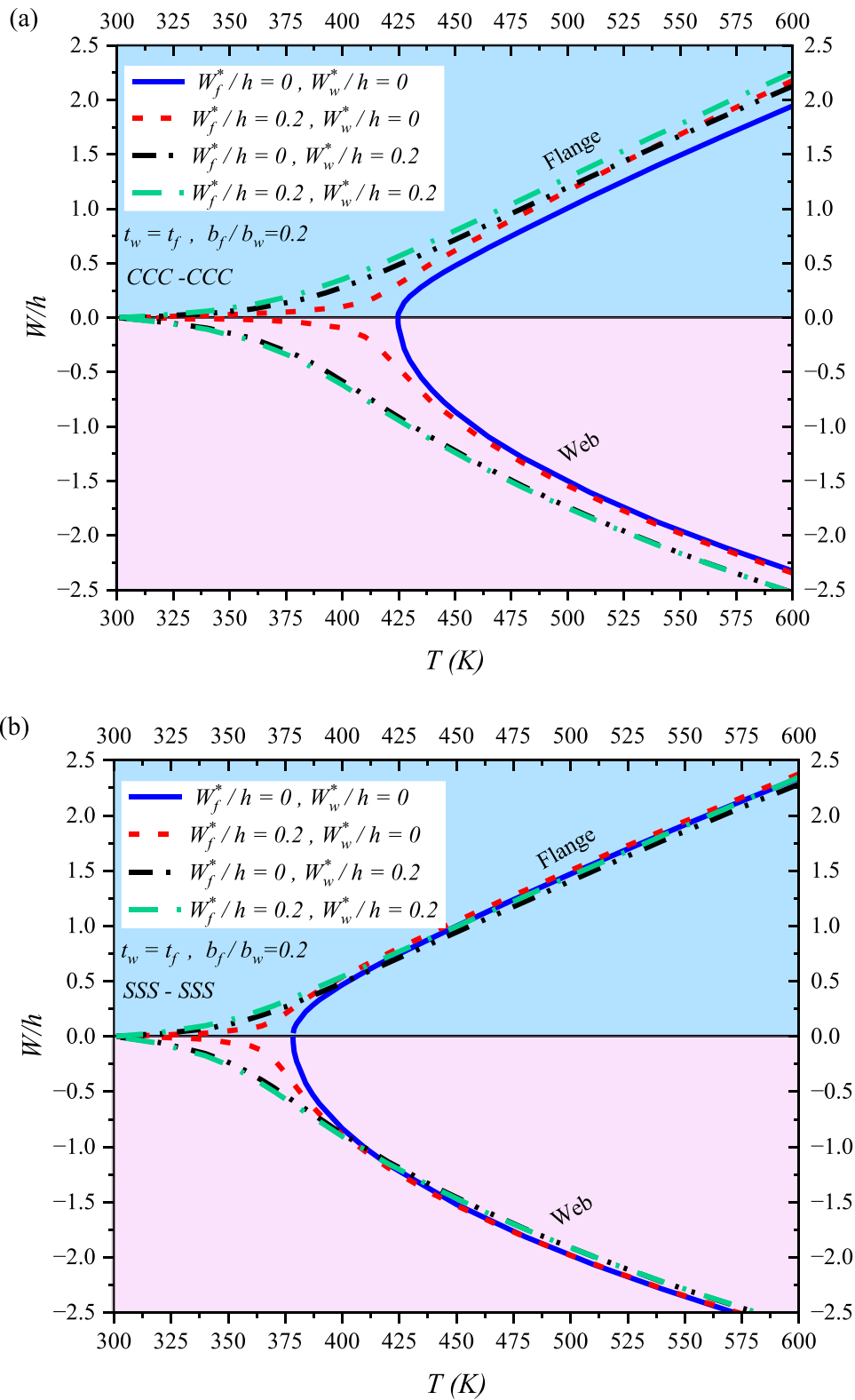
Fig. 11. Influence of geometrical imperfection on the thermal post-buckling equilibrium paths of the FGX channel section struts (a) clamped boundary condition (b) simply-supported boundary condition.

the case of clamped FGX channel section struts, it is observed that increasing the flange width from 0.2 to 0.9 leads to an approximate 30 % decrease in the fundamental frequency. This highlights the critical role of shape factors in determining the vibrational characteristics of these structures.

4.3. Imperfection sensitivity of post-buckling equilibrium paths and free vibration of FGX channel section struts

To determine the impact of geometrical imperfections on the post-buckling behavior and free vibration characteristics of channel section

struts, just the FGX graphene distribution pattern is selected as the most effective in enhancing in-plane compressive stiffness. For a thorough analysis of the impact of local geometrical imperfection, three distinct methodologies are employed to apply it. In the initial method, the web of the channel section strut is presumed to be perfect, with local geometrical imperfections applied exclusively to the flanges. This induced imperfection corresponds to the first buckling mode of the flanges, as depicted in Table 3. Conversely, in the subsequent approach, the local geometrical imperfection is exclusively applied to the web, aligning with the first mode of buckling for this component, while the flanges are assumed to be without imperfection. In the final approach, geometrical imperfections are applied simultaneously to both the flanges and the web of the channel section struts. It is crucial to emphasize that throughout the process of introducing geometrical imperfections to both the flanges and the web, the preservation of straightness at the junction is maintained as an assumption to meet the stress free edge criteria.

Fig. 11 clearly shows that under any boundary condition, the perfect FGX laminated channel section strut demonstrates a bifurcation-type instability across both the web and flange. This behavior indicates that these components stay undeformed and flat until reaching the critical temperature threshold. Conversely, the presence of geometrical imperfections initiates lateral deflections in both the flange and web right from the onset of thermal loading. An additional noteworthy observation is that the instability response of channel section struts, where imperfection is solely applied to the web, more closely resembles
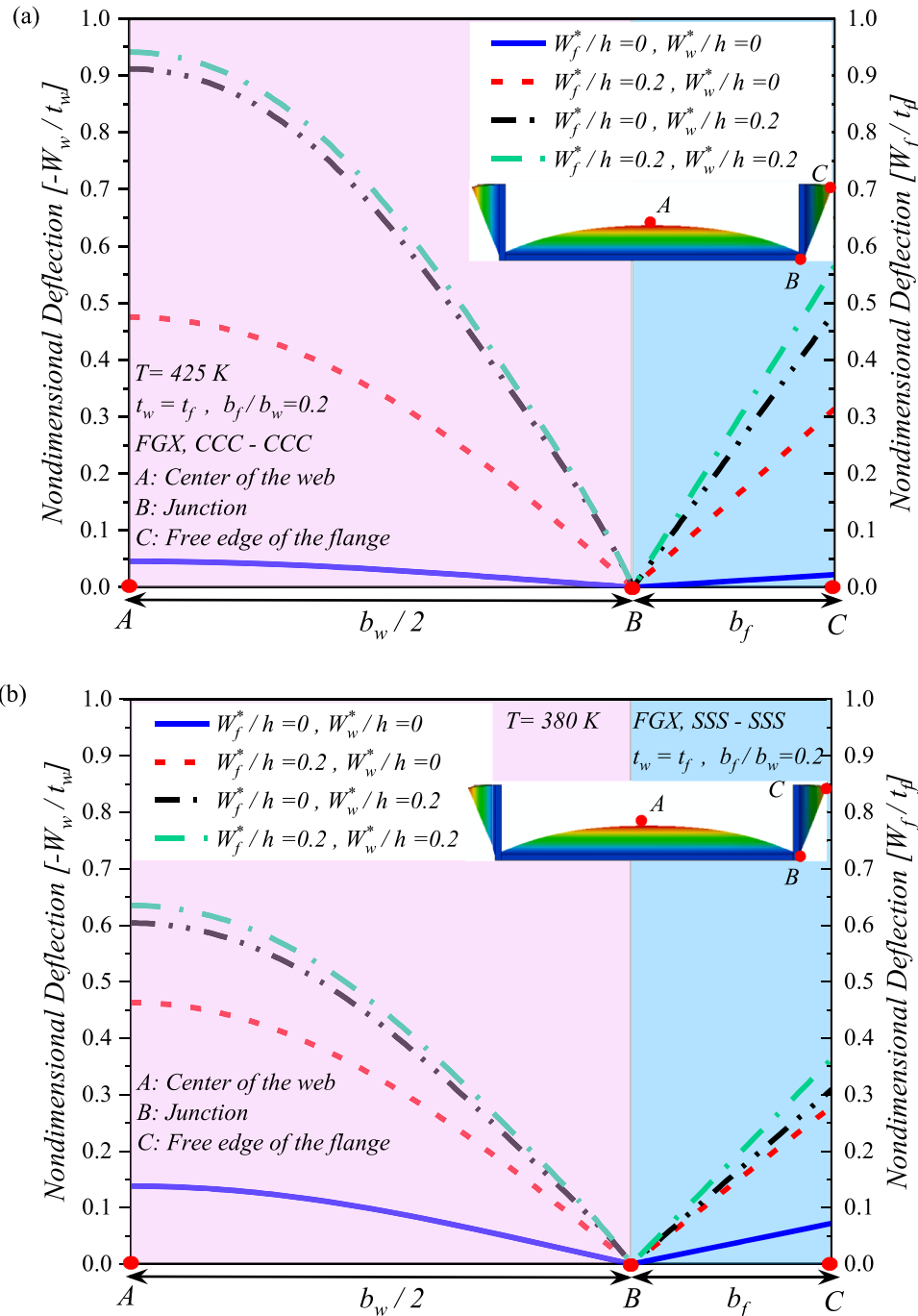
Fig. 12. Influence of geometrical imperfection on the local deflection at the buckle crest of FGX channel section struts (a) clamped boundary condition (b) simply-supported boundary condition.
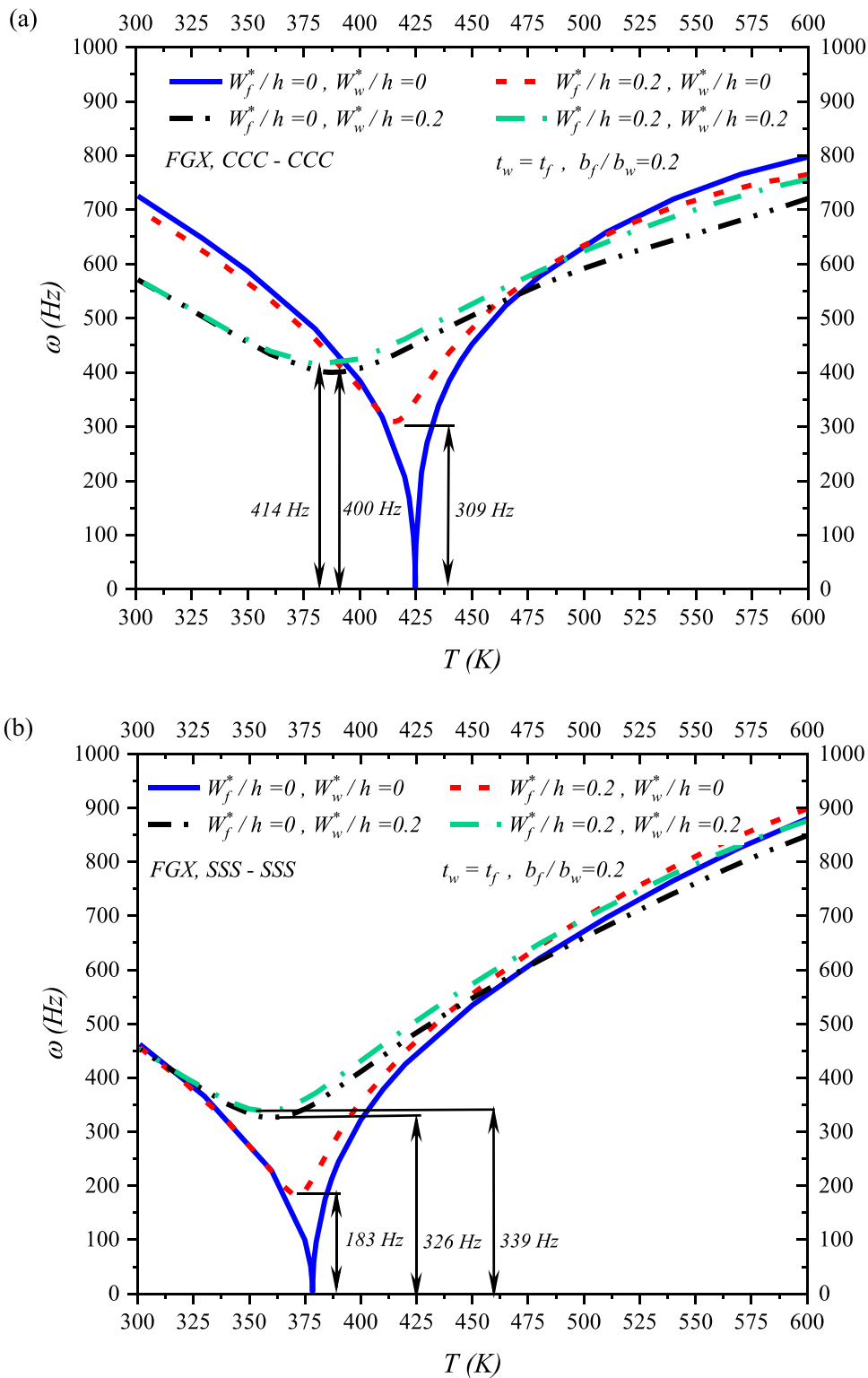
Fig. 13. Influence of geometrical imperfections on variations of thermally induced pre- and post-buckling of FGX laminated channel section struts (a) fundamental frequency with clamped boundary condition (b) fundamental frequency with simply-supported boundary condition (c) second order frequency with clamped boundary condition (d) second order with simply-supported boundary condition.
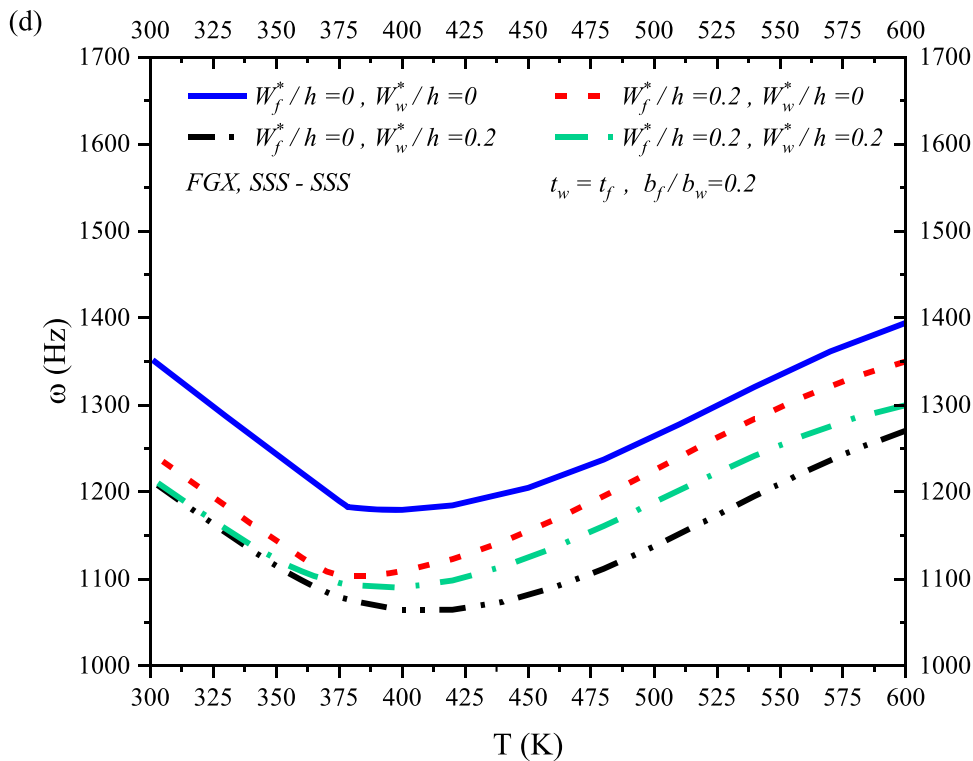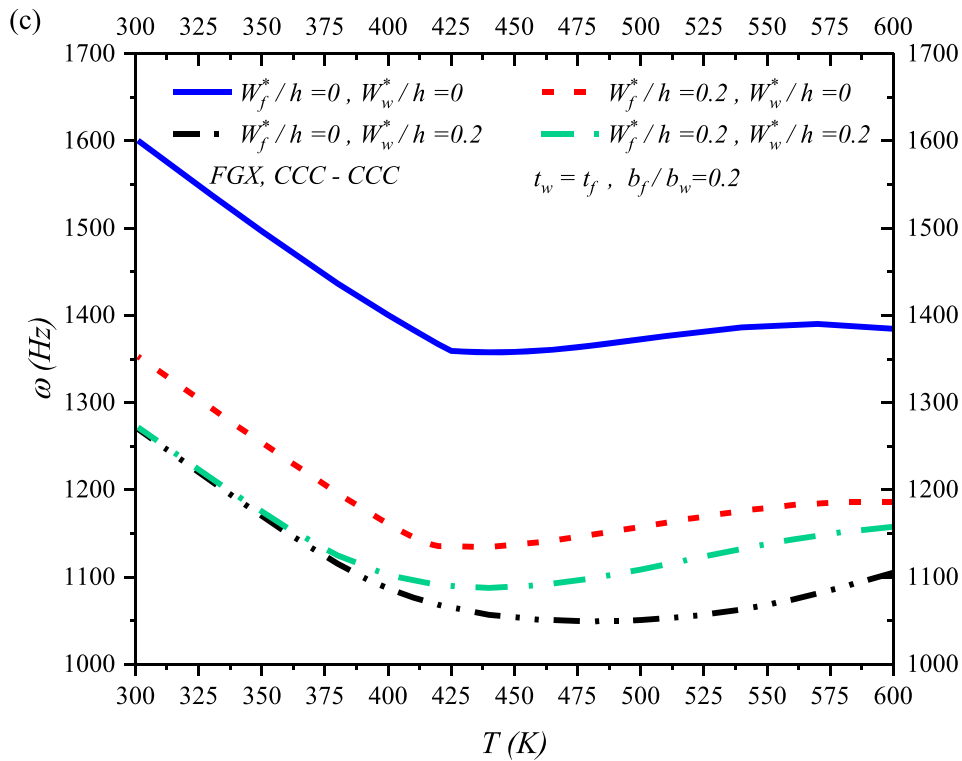
Fig. 13. (*continued*).

the scenario in which imperfections are introduced simultaneously to all segments.

A comparative analysis highlighting the effects of geometrical imperfections on the local deflection of the web and flange at the buckle crest (half length) of the channel section struts is presented in Fig. 12. Owing to the symmetry along the Z local axis of the web, as shown in Fig. 1, deflection variations are illustrated for only one half of the cross-section. It is essential to emphasize that the presented results are for temperatures $T = 450$ K and $T = 380$ K, which are very close to the critical buckling temperatures of the FGX channel section struts, under clamped and simply-supported boundary conditions, respectively. As illustrated, the deflection observed in the perfect channel section strut at temperatures marginally exceeding the critical buckling temperature is virtually insignificant when compared to scenarios incorporating

geometrical imperfections. In particular, the maximum out-of-plane displacement seen in the clamped FGX channel section strut, when it undergoes imperfections with an amplitude of $w^*/h = 0.2$ affecting both flanges and web, is approximately 2 times higher than in instance without any imperfections. It should be highlighted that the out-of-plane displacement of the flange and web is equal to zero at the junction to satisfy the in-plane stress-free edge condition.

Fig. 13 illustrates the comparison between the pre- and post-buckling free vibrations of both perfect and imperfect channel section struts. This analysis is crucial for understanding the potential effects that deviations from ideal geometrical configurations can have on the natural frequencies of FGX channel section struts with clamped and simply-supported boundary conditions.

A pivotal observation from the analysis reveals that geometrical imperfections, characterized by an amplitude of $w^*/h = 0.2$, prevent the fundamental frequencies of FGX channel section struts from diminishing to zero near the critical buckling temperature. Furthermore, introduction of these imperfections across the entire structure notably increases their fundamental frequencies in the vicinity of this critical buckling temperature. This augmentation results in enhanced frequencies, achieving up to 414 Hz for struts under clamped boundary conditions and 339 Hz for those with simply-supported boundary conditions, respectively. This phenomenon is due to the enhanced structural stiffness around the critical buckling temperature that arises from the static buckling deflection caused by the geometrical imperfection. Nevertheless, in both the pre-buckling and post-buckling phases, particularly with the clamped boundary condition, the presence of geometrical imperfections leads to a decrease in the fundamental natural frequencies. Furthermore, as clearly demonstrated in Figs. 13(c) and 13(d), the geometrical imperfections substantially diminish the second-order natural frequencies across both pre- and post-buckling states. It is important to highlight that there is no occurrence of order exchange phenomena between the first two modes of natural frequencies.

5. Concluding remarks

This research addresses the issue of laminated composite open section struts, which are commonly used in engineering, being prone to local buckling when exposed to compressive thermal loads. The investigation seeks to discover effective solutions to this problem by employing graphene sheet reinforcements. The primary objective of this study is to assess how different distributions of graphene sheet reinforcements, through the thickness of the flange and web plates of channel section struts, affect their thermal compressive instability and their pre- and post-buckling free vibration. Attention has been given to discerning the distribution patterns of graphene that most significantly enhance the critical buckling temperature and natural frequencies. Furthermore, the effect of geometrical imperfections on the nonlinear thermal compression behavior of the FG-GRC laminated channel section struts has been assessed to obtain results that more accurately reflect real-world conditions. A framework is constructed on the foundations of LW-TSDT and the von-Karman strain-displacement equation. To solve the governing equations, the minimum total potential energy principle and the Ritz method are applied in tandem with the Newton-Raphson iterative process; the obtained results are finally compared with those evaluated using the 3D finite element simulation. This study significantly enhances our comprehension of the relationship between material distribution and structural characteristics, offering pertinent insights for the development of more robust and effective engineering structures. In particular:

- Employing the FG-X graphene distribution pattern in the thickness of the web and flanges of channel section struts leads to an approximate 12 % increase in the critical buckling temperature for clamped channel section struts, compared to those using the FGO graphene distribution pattern. For cases with simply-supported boundary conditions, this increase is approximately 9 %.

- This study reveals that within the shape factor, $b_f/b_w = 0.2$, analyzed, altering the graphene distribution patterns through the thickness of the flanges, while maintaining a constant graphene distribution in the web, has a minimal effect on the critical buckling temperature of channel section struts. The maximum relative differences observed are approximately 1.13 % for clamped boundary conditions and 2 % for simply-supported boundary conditions.

- Conversely, modifying the graphene distribution patterns in the web, while reinforcing the flanges with a consistent type of graphene sheet, can change the critical buckling temperature by up to 12 %. This indicates that, for the specific shape factor considered, the buckling behavior of the web plays a dominant role in the overall instability response of channel section struts.

- The analysis of thermally induced pre- and post-buckling free vibration in channel section struts, which are reinforced with different graphene distribution patterns, demonstrates that, through the pre-buckling situation, struts featuring the FGX channel section configurations achieve the highest natural frequencies. However, this pattern alters in the post-buckling stage.

- Introducing the same magnitude of geometrical imperfections to both the flanges and web of channel section struts, reinforced with FGX graphene distribution patterns, leads to an increase in the fundamental frequency by about 400 Hz near the critical buckling temperature of $T = 425$ K.

- The enhancement of natural frequencies in FG-GRC laminated channel section struts through the post-buckling states, as a result of uniform temperature increase, can be attributed to the dominance of the stiffening effect, which is a consequence of static buckling deflection, over the softening effect caused by thermal stress.

- The equilibrium path of perfect FG-GRC channel section struts typically follows a primary-secondary trajectory, wherein the out-of-plane displacement remains unchanged with increasing temperature up to the instability point, at which the structure deflects. However, the introduction of geometrical imperfections initiates deformation from the onset of thermal loading, thereby leading to an unique equilibrium path.

- Incorporating an asymmetric graphene distribution pattern (FGV) or introducing geometrical imperfections that induce a bending moment throughout the structure from the initial stages of thermal loading effectively prevents the fundamental natural frequencies of FG-GRC channel section struts from reaching zero in proximity to the critical buckling temperature.

CRediT authorship contribution statement

S.F. Nikrad: Formal analysis, Conceptualization. **A.H. Akbarzadeh:** Supervision. **M. Bodaghi:** Writing – review & editing. **M. Hamidinejad:** Supervision. **Z.T. Chen:** Supervision.

Declaration of competing interest

The authors declare that they have no known competing financial interests or personal relationships that could have appeared to influence the work reported in this paper.

Data availability

No data was used for the research described in the article.

Appendix A

According to the TSDT, the normal and transverse shear strain tensors of the FG-GRC laminated plate can be written as [51]:

$$
\left\{\begin{matrix} \varepsilon_{xx} \\ \varepsilon_{yy} \\ \gamma_{xy} \end{matrix}\right\}_j^i = \left\{\begin{matrix} \varepsilon_{xx}^{(0)} \\ \varepsilon_{yy}^{(0)} \\ \gamma_{xy}^{(0)} \end{matrix}\right\}_j^i + z \left\{\begin{matrix} \varepsilon_{xx}^{(1)} \\ \varepsilon_{yy}^{(1)} \\ \gamma_{xy}^{(1)} \end{matrix}\right\}_j^i + z^3 \left\{\begin{matrix} \varepsilon_{xx}^{(3)} \\ \varepsilon_{yy}^{(3)} \\ \gamma_{xy}^{(3)} \end{matrix}\right\}_j^i
$$

$$
\left\{\begin{matrix} \gamma_{yz} \\ \gamma_{xz} \end{matrix}\right\}_j^i = \left\{\begin{matrix} \gamma_{yz}^{(0)} \\ \gamma_{xz}^{(0)} \end{matrix}\right\}_j^i + z^2 \left\{\begin{matrix} \gamma_{yz}^{(2)} \\ \gamma_{xz}^{(2)} \end{matrix}\right\}_j^i \tag{A.1}
$$

where:

$$
\left\{\begin{matrix} \varepsilon_{xx}^{(0)} \\ \varepsilon_{yy}^{(0)} \\ \gamma_{xy}^{(0)} \end{matrix}\right\}_j^i = \left\{\begin{matrix} \frac{\partial u_0}{\partial x} + \left(\frac{1}{2}\right)\left(\frac{\partial w_0}{\partial x}\right)^2 + \left(\frac{\partial w_0}{\partial x}\right)\left(\frac{\partial w^*}{\partial x}\right) \\ \frac{\partial v_0}{\partial y} + \left(\frac{1}{2}\right)\left(\frac{\partial w_0}{\partial y}\right)^2 + \left(\frac{\partial w_0}{\partial y}\right)\left(\frac{\partial w^*}{\partial y}\right) \\ \frac{\partial u_0}{\partial y} + \frac{\partial v_0}{\partial x} + \frac{\partial w_0}{\partial x}\frac{\partial w^*}{\partial y} + \frac{\partial w_0}{\partial y}\frac{\partial w^*}{\partial x} \end{matrix}\right\}_j^i
$$

$$
\left\{\begin{matrix} \varepsilon_{xx}^{(1)} \\ \varepsilon_{yy}^{(1)} \\ \gamma_{xy}^{(1)} \end{matrix}\right\}_j^i = \left\{\begin{matrix} \frac{\partial \varphi_x}{\partial x} \\ \frac{\partial \varphi_y}{\partial y} \\ \frac{\partial \varphi_x}{\partial y} + \frac{\partial \varphi_y}{\partial x} \end{matrix}\right\}_j^i
$$

$$
\left\{\begin{matrix} \varepsilon_{xx}^{(3)} \\ \varepsilon_{yy}^{(3)} \\ \gamma_{xy}^{(3)} \end{matrix}\right\}_j^i = \left\{\begin{matrix} \left(\frac{-4}{3h^2}\right)\left(\frac{\partial \varphi_x}{\partial x} + \frac{\partial^2 w_0}{\partial x^2}\right) \\ \left(\frac{-4}{3h^2}\right)\left(\frac{\partial \varphi_y}{\partial y} + \frac{\partial^2 w_0}{\partial y^2}\right) \\ \left(\frac{-4}{3h^2}\right)\left(\frac{\partial \varphi_x}{\partial y} + \frac{\partial \varphi_y}{\partial x} + 2\frac{\partial^2 w_0}{\partial x \partial y}\right) \end{matrix}\right\}_j^i
$$

$$
\left\{\begin{matrix} \gamma_{yz}^{(0)} \\ \gamma_{xz}^{(0)} \end{matrix}\right\}_j^i = \left\{\begin{matrix} \varphi_y + \frac{\partial w_0}{\partial y} \\ \varphi_x + \frac{\partial w_0}{\partial x} \end{matrix}\right\}_j^i, \quad \left\{\begin{matrix} \gamma_{yz}^{(2)} \\ \gamma_{xz}^{(2)} \end{matrix}\right\}_j^i = \left(\frac{-4}{h^2}\right)\left\{\begin{matrix} \gamma_{yz}^{(0)} \\ \gamma_{xz}^{(0)} \end{matrix}\right\}_j^i \tag{A.2}
$$

By assuming linear stress-strain relations we have [75]:

$$
\begin{bmatrix} \sigma_{xx} \\ \sigma_{yy} \\ \tau_{yz} \\ \tau_{xz} \\ \tau_{xy} \end{bmatrix}_j^i = \begin{bmatrix} \overline{Q}_{11} & \overline{Q}_{12} & 0 & 0 & \overline{Q}_{16} \\ \overline{Q}_{21} & \overline{Q}_{22} & 0 & 0 & \overline{Q}_{26} \\ 0 & 0 & \overline{Q}_{44} & \overline{Q}_{45} & 0 \\ 0 & 0 & \overline{Q}_{45} & \overline{Q}_{55} & 0 \\ \overline{Q}_{61} & \overline{Q}_{62} & 0 & 0 & \overline{Q}_{66} \end{bmatrix}_j^i \left(\begin{bmatrix} \varepsilon_{xx} \\ \varepsilon_{yy} \\ \gamma_{yz} \\ \gamma_{xz} \\ \gamma_{xy} \end{bmatrix}\right)_j^i \tag{A.3}
$$

Based on the transformation rule in the fiber reinforced composite materials, $\overline{Q}_j^i$ denotes the transformed elastic constants.

According to TSDT, the stress resultants $N_j^i, M_j^i, P_j^i, Q_j^i,$ and R_j^i are defined by:

$$
\left\{\begin{matrix} \{N\} \\ \{M\} \\ \{P\} \end{matrix}\right\}_j^i = \begin{bmatrix} [A] & [B] & [E] \\ [B] & [D] & [F] \\ [E] & [F] & [H] \end{bmatrix}_j^i \left\{\begin{matrix} \{\varepsilon^0\} \\ \{\varepsilon^1\} \\ \{\varepsilon^3\} \end{matrix}\right\}_j^i
$$

$$
\left\{\begin{matrix} \{Q\} \\ \{R\} \end{matrix}\right\}_j^i = \begin{bmatrix} [As] & [Ds] \\ [Ds] & [Fs] \end{bmatrix}_j^i \left\{\begin{matrix} \{\gamma^0\} \\ \{\gamma^2\} \end{matrix}\right\}_j^i \tag{A.4}
$$

The stiffness matrices in Eq. (3) are defined as:

$$\left(A_j^i, B_j^i, D_j^i, E_j^i, F_j^i, H_j^i\right) = \int_{\frac{-h}{2}}^{\frac{h}{2}} \overline{Q}_j^i \left(1, z, z^2, z^3, z^4, z^6\right) dz, \ (i,j = 1, 2, 6)$$

$$\left(As_j^i, Ds_j^i, Fs_j^i\right) = \int_{\frac{-h}{2}}^{\frac{h}{2}} \overline{Q}_j^i \left(1, z^2, z^4\right) dz, \ (i,j = 4, 5) \tag{A.5}$$

Appendix B

$$\varphi_{w,x}^{(1)} = \sum_{j=0}^{J} \sum_{k=0}^{K} \varnothing_{wx,jk}^{(1)} x^j y^k$$

$$\vdots$$

$$\varphi_{w,x}^{(n)} = \sum_{j=0}^{J} \sum_{k=0}^{K} \varnothing_{wx,jk}^{(n)} x^j y^k$$

$$\varphi_{f1,x}^{(1)} = \left[\sum_{j=0}^{J} \sum_{k=0}^{K} \left(y' + \frac{b_{f1}}{2}\right) \varnothing_{f1x,jk}^{(1)} x^j y^k \right] + \varphi_{w,x}^{(1)}\left(x, \frac{b_w}{2}\right)$$

$$\vdots$$

$$\varphi_{f1,x}^{(n)} = \left[\sum_{j=0}^{J} \sum_{k=0}^{K} \left(y' + \frac{b_{f1}}{2}\right) \varnothing_{f1x,jk}^{(n)} x^j y^k \right] + \varphi_{w,x}^{(n)}\left(x, \frac{b_w}{2}\right)$$

$$\varphi_{f2,x}^{(1)} = \left[\sum_{j=0}^{J} \sum_{k=0}^{K} \left(y'' - \frac{b_f}{2}\right) \varnothing_{f2x,jk}^{(1)} x^j y^k \right] + \varphi_{w,x}^{(1)}\left(x, \frac{-b_w}{2}\right)$$

$$\vdots$$

$$\varphi_{f2,x}^{(n)} = \left[\sum_{j=0}^{J} \sum_{k=0}^{K} \left(y'' - \frac{b_f}{2}\right) \varnothing_{f2x,jk}^{(n)} x^j y^k \right] + \varphi_{w,x}^{(n)}\left(x, \frac{-b_w}{2}\right) \tag{B.1}$$

References

[1] S. Stankovich, Graphene-based composite materials, Nature 442 (7100) (2006) 282–286.

[2] J.R. Potts, D.R. Dreyer, C.W. Bielawski, R.S. Ruoff, Graphene-based polymer nanocomposites, Polymer. (Guildf) 52 (1) (2011) 5–25, https://doi.org/10.1016/j.polymer.2010.11.042.

[3] T.K. Das, S. Prusty, Graphene-based polymer composites and their applications, Polym. Plast. Technol. Eng. 52 (4) (2013) 319–331.

[4] M.K. Blees, Graphene kirigami, Nature 524 (7564) (2015) 204–207.

[5] J. Cai, A. Akbarzadeh, Hierarchical kirigami-inspired graphene and carbon nanotube metamaterials: tunability of thermo-mechanic properties, Mater. Des. 206 (2021) 109811.

[6] H. Ghasemi, A. Rajabpour, A.H. Akbarzadeh, Tuning thermal conductivity of porous graphene by pore topology engineering: comparison of non-equilibrium molecular dynamics and finite element study, Int. J. Heat. Mass Transf. 123 (2018) 261–271, https://doi.org/10.1016/j.ijheatmasstransfer.2018.02.094.

[7] K.S. Novoselov, Electric Field Effect in Atomically Thin Carbon Films, et al., Kluwer, 2000 [Online]. Available: www.arXiv.org/quant-ph/.

[8] M.D. Stoller, S. Park, Z. Yanwu, J. An, R.S. Ruoff, Graphene-Based ultracapacitors, Nano Lett. 8 (10) (2008) 3498–3502, https://doi.org/10.1021/nl802558y. Oct.

[9] R.R. Nair, Fine structure constant defines visual transparency of graphene, Science (1979) 320 (5881) (2008) 1308, https://doi.org/10.1126/science.1156965. Jun.

[10] C. Lee, X. Wei, J.W. Kysar, J. Hone, Measurement of the elastic properties and intrinsic strength of monolayer graphene, Science (1979) 321 (5887) (2008) 385–388.

[11] A.A. Balandin, Superior thermal conductivity of single-layer graphene, Nano Lett. 8 (3) (2008) 902–907, https://doi.org/10.1021/nl0731872. Mar.

[12] C.D. Reddy, S. Rajendran, K.M. Liew, Equilibrium configuration and continuum elastic properties of finite sized graphene, Nanotechnology. 17 (3) (2006) 864.

[13] F. Scarpa, S. Adhikari, A.S. Phani, Effective elastic mechanical properties of single layer graphene sheets, Nanotechnology. 20 (6) (2009) 065709.

[14] A.B. Alencar, A.P.M. Barboza, B.S. Archanjo, H. Chacham, B.R.A. Neves, Experimental and theoretical investigations of monolayer and fewlayer talc, 2d. Mater. 2 (1) (2015), https://doi.org/10.1088/2053-1583/2/1/015004. Feb.

[15] R. Atif, F. Inam, Modeling and simulation of graphene based polymer nanocomposites: advances in the last decade, Graphene 05 (02) (2016) 96–142, https://doi.org/10.4236/graphene.2016.52011.

[16] P. Koskinen T. Korhonen, "Plenty of motion at the bottom: atomically thin liquid gold membrane".

[17] S. Park, R.S. Ruoff, Chemical methods for the production of graphenes, Nat. Nanotechnol. 4 (4) (2009) 217–224.

[18] Y. Magnin, G.D. Förster, F. Rabilloud, F. Calvo, A. Zappelli, C. Bichara, Thermal expansion of free-standing graphene: benchmarking semi-empirical potentials, J. Phys. Condensed Matter. 26 (18) (2014), https://doi.org/10.1088/0953-8984/26/18/185401. May.

[19] D.G. Papageorgiou, I.A. Kinloch, R.J. Young, Mechanical properties of graphene and graphene-based nanocomposites, in: Progress in Materials Science, 90, Elsevier Ltd, 2017, pp. 75–127, https://doi.org/10.1016/j.pmatsci.2017.07.004. Oct. 01.

[20] M.A. Milani, Polypropylene/graphene nanosheet nanocomposites by in situ polymerization: synthesis, characterization and fundamental properties, Compos. Sci. Technol. 84 (2013) 1–7.

[21] M. Salomäki, J. Kauppila, J. Kankare, J. Lukkari, Oxidative layer-by-layer multilayers based on metal coordination: influence of intervening graphene oxide layers, Langmuir. 34 (44) (2018) 13171–13182, https://doi.org/10.1021/acs.langmuir.8b02784. Nov.

[22] D.D. Kulkarni, I. Choi, S.S. Singamaneni, V.V. Tsukruk, Graphene oxide–polyelectrolyte nanomembranes, ACS. Nano 4 (8) (2010) 4667–4676.

[23] S. Zhao, Z. Zhao, Z. Yang, L. Ke, S. Kitipornchai, J. Yang, Functionally graded graphene reinforced composite structures: a review, Eng. Struct. 210 (2020) 110339.

[24] M.A. Rafiee, J. Rafiee, Z.Z. Yu, N. Koratkar, Buckling resistant graphene nanocomposites, Appl. Phys. Lett. 95 (22) (2009) 223103.

[25] C. Feng, S. Kitipornchai, J. Yang, Nonlinear bending of polymer nanocomposite beams reinforced with non-uniformly distributed graphene platelets (GPLs), Compos. B Eng. 110 (2017) 132–140.

[26] J. Yang, H. Wu, S. Kitipornchai, Buckling and postbuckling of functionally graded multilayer graphene platelet-reinforced composite beams, Compos. Struct. 161 (2017) 111–118.

[27] H. Wu, J. Yang, S. Kitipornchai, Dynamic instability of functionally graded multilayer graphene nanocomposite beams in thermal environment, Compos. Struct. 162 (2017) 244–254.

[28] H.-S. Shen, F. Lin, Y. Xiang, Nonlinear bending and thermal postbuckling of functionally graded graphene-reinforced composite laminated beams resting on elastic foundations, Eng. Struct. 140 (2017) 89–97.

[29] S. Zhao, Z. Yang, S. Kitipornchai, J. Yang, Dynamic instability of functionally graded porous arches reinforced by graphene platelets, Thin-Walled Struct. 147 (2020) 106491.

[30] A. Parashar, P. Mertiny, Representative volume element to estimate buckling behavior of graphene/polymer nanocomposite, Nanoscale Res. Lett. 7 (1) (2012) 1–6.

[31] H.-S. Shen, Y. Xiang, F. Lin, D. Hui, Buckling and postbuckling of functionally graded graphene-reinforced composite laminated plates in thermal environments, Compos. B Eng. 119 (2017) 67–78.

[32] H.-S. Shen, Y. Xiang, F. Lin, Nonlinear bending of functionally graded graphene-reinforced composite laminated plates resting on elastic foundations in thermal environments, Compos. Struct. 170 (2017) 80–90.

[33] R. Ma, Q. Jin, Stability of functionally graded graphene-reinforced composite laminated thick plates in thermal environment, Acta Mech. 233 (10) (2022) 3977–3996.

[34] Y. Kiani, NURBS-based isogeometric thermal postbuckling analysis of temperature dependent graphene reinforced composite laminated plates, Thin-Walled Struct. 125 (2018) 211–219.

[35] S.F. Nikrad, Z.T. Chen, A.H. Akbarzadeh, Nonlinear thermal postbuckling of functionally graded graphene-reinforced composite laminated plates with circular or elliptical delamination, Acta Mech. (2023), https://doi.org/10.1007/s00707-023-03694-0.

[36] H.-S. Shen, Y. Xiang, F. Lin, Nonlinear vibration of functionally graded graphene-reinforced composite laminated plates in thermal environments, Comput. Methods Appl. Mech. Eng. 319 (2017) 175–193.

[37] S.F. Nikrad, Z.T. Chen, A.H. Akbarzadeh, Effect of graphene reinforcement distribution on energy release rate and vibration of thermally pre/post-buckled delaminated composite plates, Thin-Walled Struct. 189 (2023) 110876, https://doi.org/10.1016/j.tws.2023.110876.

[38] B. Saiah, M. Bachene, M. Guemana, Y. Chiker, B. Attaf, On the free vibration behavior of nanocomposite laminated plates contained piece-wise functionally graded graphene-reinforced composite plies, Eng. Struct. 253 (2022) 113784, https://doi.org/10.1016/j.engstruct.2021.113784.

[39] H. Niknam, A.H. Akbarzadeh, Graded lattice structures: simultaneous enhancement in stiffness and energy absorption, Mater. Des. 196 (2020) 109129, https://doi.org/10.1016/j.matdes.2020.109129.

[40] H.Yazdani Sarvestani, A.H. Akbarzadeh, H. Niknam, K. Hermenean, 3D printed architected polymeric sandwich panels: energy absorption and structural performance, Compos. Struct. 200 (2018) 886–909, https://doi.org/10.1016/j.compstruct.2018.04.002.

[41] J. Cai, H. Chen, Y. Li, A. Akbarzadeh, Lessons from nature for carbon-based nanoarchitected metamaterials, Small. Sci. 2 (12) (2022) 2200039, https://doi.org/10.1002/smsc.202200039. Dec.

[42] X. Chen, H.S. Shen, X.H. Huang, Thermo-mechanical postbuckling analysis of sandwich plates with functionally graded auxetic GRMMC core on elastic foundations, Compos. Struct. 279 (2022) 114796.

[43] X. Chen, H.S. Shen, Thermo-mechanical postbuckling analysis of sandwich cylindrical panels with functionally graded auxetic GRMMC core supported by elastic foundations, Ocean Eng. 247 (2022) 110661, https://doi.org/10.1016/j.oceaneng.2022.110661.

[44] X. Chen, H.-S. Shen, Y. Xiang, Thermo-mechanical postbuckling analysis of sandwich cylindrical shells with functionally graded auxetic GRMMC core surrounded by an elastic medium, Thin-Walled Struct. 171 (2022) 108755, https://doi.org/10.1016/j.tws.2021.108755.

[45] L. Yan, B. Yang, J. Cai, S. Lin, A. Akbarzadeh, Multiscale functionalized graphene origami metamaterials enable programming thermoelectric performance of flexible energy harvesters, Carbon. N. Y. 225 (2024) 119–149, https://doi.org/10.1016/j.carbon.2024.119149.

[46] D. Ho, H.S. Park, S.Y. Kim, U. Schwingenschlögl, Graphene origami with highly tunable coefficient of thermal expansion, ACS. Nano 14 (2020) 8969–8974, https://doi.org/10.1021/acsnano.0c03791.

[47] H.Y. Sarvestani, A.H. Akbarzadeh, H. Niknam, K. Hermenean, 3D printed architected polymeric sandwich panels: energy absorption and structural performance, Compos. Struct. 200 (2018) 886–909, https://doi.org/10.1016/j.compstruct.2018.04.002. Se.

[48] H. Younes, X. Kuang, D. Lou, B. DeVries, M.M. Rahman, H. Hong, Magnetic-field-assisted DLP stereolithography for controlled production of highly aligned 3D printed polymer-Fe3O4@graphene nanocomposites, Mater. Res. Bull. 154 (2022), https://doi.org/10.1016/j.materresbull.2022.111938. Oct.

[49] H.R. Ovesy, S.A.M. Ghannadpour, An exact finite strip for the initial postbuckling analysis of channel section struts, Comput. Struct. (2011) 1785–1796, https://doi.org/10.1016/j.compstruc.2010.10.009. Oct.

[50] J.L. Dawe, G.L. Kulak, /Members, "Local buckling of w shape columns and beams".

[51] P.K. Basu M.N. Akhtar, "Interactive and local buckling of thin-walled members," 1991.

[52] J. Loughlan, N. Yidris, The local-overall flexural interaction of fixed-ended plain channel columns and the influence on behaviour of local conditions at the constituent plate ends, Thin-Walled Struct. 81 (2014) 132–137, https://doi.org/10.1016/j.tws.2014.02.028.

[53] S.F. Nikrad, H. Asadi, T. Ozbakkaloglu, Compressive instability of open section nanocomposite struts using a layerwise theory, Comput. Methods Appl. Mech. Eng. 355 (2019) 820–839, https://doi.org/10.1016/j.cma.2019.07.001. Oct.

[54] B.T. John DeWolf, T. Peokoz, A. Members, G. Winter, H.M. Asce, "Journal of the structural division local and overall buckling of cold-formed members".

[55] P. Schreiber, C. Mittelstedt, A holistic approach for local buckling of composite laminated beams under compressive load, Arch.Appl. Mech. 89 (7) (2019) 1243–1257, https://doi.org/10.1007/s00419-018-1496-1. Jul.

[56] L. Szló P. Kollá, "Local buckling of fiber reinforced plastic composite structural members with open and closed cross sections", https://doi.org/10.1061/ASCE0733-94452003129:111503.

[57] S.F. Nikrad, H. Asadi, Q. Wang, Postbuckling behaviors of open section composite struts with edge delamination using a layerwise theory, Int. J. Non. Linear. Mech. 95 (2017) 315–326, https://doi.org/10.1016/j.ijnonlinmec.2017.07.006. Oct.

[58] P. Qiao, M. Asce, G. Zou, "Local buckling of elastically restrained fiber-reinforced plastic plates and its application to box sections", https://doi.org/10.1061/ASCE0733-93392002128:121324.

[59] J. Loughlan, N. Yidris, P.R. Cunningham, The effects of local buckling and material yielding on the axial stiffness and failure of uniformly compressed I-section and box-section struts, Thin-Wall. Struct. 49 (2) (2011) 264–279, https://doi.org/10.1016/j.tws.2010.11.004. Feb.

[60] J. Chen, Y. He, W.L. Jin, Stub column tests of thin-walled complex section with intermediate stiffeners, Thin-Wall. Struct. 48 (6) (2010) 423–429, https://doi.org/10.1016/j.tws.2010.01.008. Jun.

[61] S.A.M. Ghannadpour, H.R. Ovesy, An exact finite strip for the calculation of relative post-buckling stiffness of I-section struts, Int. J. Mech. Sci. 50 (9) (2008) 1354–1364, https://doi.org/10.1016/j.ijmecsci.2008.07.010.

[62] C. Mittelstedt, Local buckling of wide-flange thin-walled anisotropic composite beams, Arch. Appl. Mech. 77 (7) (2007) 439–452, https://doi.org/10.1007/s00419-006-0102-0. Jul.

[63] J. Rhodes, J.M. Harvey, Plain Channel Section Struts in Compression And Bending Beyond the Local Buckling Load, Pergamon Press, 1976.

[64] H.R. Ovesy, J. Loughlan, S.A.M. GhannadPour, G. Morada, Geometric non-linear analysis of box sections under end shortening, using three different versions of the finite-strip method, Thin-Wall. Struct. 44 (6) (2006) 623–637, https://doi.org/10.1016/j.tws.2006.05.006.

[65] H.R. Ovesy, J. Loughlan, S.A.M. GhannadPour, Geometric non-linear analysis of channel sections under end shortening, using different versions of the finite strip method, Comput. Struct. 84 (13–14) (2006) 855–872, https://doi.org/10.1016/j.compstruc.2006.02.010. May.

[66] J. Rhodes, "Buckling of thin plates and members-and early work on rectangular tubes," 2002. [Online]. Available: www.elsevier.com/locate/tws.

[67] T.R. Graves Smith, The Effect of Initial Imperfections on the Strength of Thin-Walled Box Columns, Pergamon Press, 1971.

[68] P. Rozylo, K. Falkowicz, Numerical analysis of the behavior of compressed thin-walled elements with holes, Adv. Sci. Technol. Res. J 10 (2020) 199–206, https://doi.org/10.1016/j.compstruct.2020.112716.

[69] K. Falkowicz, Experimental and numerical failure analysis of thin-walled composite plates using progressive failure analysis, Compos. Struct. 305 (2016) 116474, https://doi.org/10.12913/22998624/64006.

[70] P. Wysmulski, H. Debski, K. Falkowicz, Sensitivity of compressed composite channel columns to eccentric loading, Materials. (Basel) 15 (19) (2022), https://doi.org/10.3390/ma15196938. Oct.

[71] K. Falkowicz, P. Wysmulski, H. Debski, Buckling Analysis of Laminated Plates with Asymmetric Layup by Approximation Method, Materials. (Basel) 16 (14) (2023), https://doi.org/10.3390/ma16144948. Jul.

[72] K. Falkowicz, H. Dębski, The work of a compressed, composite plate in asymmetrical arrangement of layers, in: AIP Conference Proceedings, American Institute of Physics Inc., 2019, https://doi.org/10.1063/1.5092008. Mar.

[73] H. Debski, P. Rozylo, K. Falkowicz, Stability and load-carrying capacity of short open-section composite columns under eccentric compression loading, Compos. Struct. 252 (2020) 112716, https://doi.org/10.1016/j.compstruct.2020.112716.

[74] P. Rozylo, K. Falkowicz, Stability and failure analysis of compressed thin-walled composite structures with central cut-out, using three advanced independent damage models, Compos. Struct. 273 (2021) 114298, https://doi.org/10.1016/j.compstruct.2021.114298.

[75] F. Lin, Y. Xiang, H.S. Shen, Temperature dependent mechanical properties of graphene reinforced polymer nanocomposites – A molecular dynamics simulation, Compos. B Eng. 111 (2017) 261–269, https://doi.org/10.1016/j.compositesb.2016.12.004.

[76] J.C.H. Affdl, J.L. Kardos, The Halpin-Tsai equations: a review, Polym. Eng. Sci. 16 (5) (1976) 344–352, https://doi.org/10.1002/pen.760160512. May.

[77] H.-S. Shen, Y. Xiang, J.N. Reddy, Thermal postbuckling behavior of FG-GRC laminated cylindrical panels with temperature-dependent properties, Compos. Struct. 211 (2019) 433–442, https://doi.org/10.1016/j.compstruct.2018.12.023.

[78] J.N. Reddy, Mechanics of Laminated Composite Plates and Shells, CRC Press, 2003.

[79] M. Kharazi, H.R. Ovesy, M. Asghari Mooneghi, Buckling analysis of delaminated composite plates using a novel layerwise theory, Thin-Walled Struct. 74 (2014) 246–254, https://doi.org/10.1016/j.tws.2013.08.008.

[80] S. Kitipornchai, J. Yang, K.M. Liew, Semi-analytical solution for nonlinear vibration of laminated FGM plates with geometric imperfections, Int. J. Solids. Struct. 41 (9) (2004) 2235–2257, https://doi.org/10.1016/j.ijsolstr.2003.12.019.

[81] S.F. Nikrad, H. Asadi, Thermal postbuckling analysis of temperature dependent delaminated composite plates, Thin-Walled Struct. 97 (2015) 296–307, https://doi.org/10.1016/j.tws.2015.09.027.